Nanoscale Advances

REVIEW

View Article Online
View Journal | View Issue

Check for updates

Cite this: *Nanoscale Adv.*, 2021, **3**, 5525

Nanomaterials for the electrochemical nitrogen reduction reaction under ambient conditions

Juan Wen,[a] Linqing Zuo,[a] Haodong Sun,[a] Xiongwei Wu,[b] Ting Huang,[a] Zaichun Liu,[a] Jing Wang,*[a] Lili Liu,*[a] Yuping Wu,*[a] Xiang Liu[a] and Teunis van Ree[c]

As an important chemical product and carbon-free energy carrier, ammonia has a wide range of daily applications in several related fields. Although the industrial synthesis method using the Haber–Bosch process could meet production demands, its huge energy consumption and gas emission limit its long-time development. Therefore, the clean and sustainable electrocatalytic N_2 reduction reaction (NRR) operating under conditions have attracted great attention in recent years. However, the chemical inertness of N_2 molecules makes it difficult for this reaction to proceed. Therefore, rationally designed catalysts need to be introduced to activate N_2 molecules. Here, we summarize the recent progress in low-dimensional nanocatalyst development, including the relationship between the structure and NRR performance from both the theoretical and experimental perspectives. Some insights into the development of NRR electrocatalysts from electronic control aspects are provided. In addition, the theoretical mechanisms, reaction pathways and credibility studies of the NRR are discussed. Some challenges and future prospects of the NRR are also pointed out.

Received 8th June 2021
Accepted 26th July 2021

DOI: 10.1039/d1na00426c

rsc.li/nanoscale-advances

Open Access Article. Published on 13 1400. Downloaded on 14/02/1405 07:56:34 ..
This article is licensed under a Creative Commons Attribution-NonCommercial 3.0 Unported Licence.

[a]*State Key Laboratory of Materials-oriented Chemical Engineering, School of Energy Science and Engineering, Institute for Advanced Materials, Nanjing Tech University, Nanjing 211816, China. E-mail: wuyp@njtech.edu.cn; wjx2015@njtech.edu.cn*
[b]*College of Chemistry and Materials, Hunan Agriculture University, Changsha, Hunan 410128, China*
[c]*Department of Chemistry, University of Venda, Thohoyandou 0950, South Africa*

Yuping Wu, FRSC, Distinguished Professor of Nanjing Tech University, received his Ph. D. degree from the Institute of Chemistry, CAS, in 1997. In 2003, he was promoted to full professor in Fudan University, China. In 2015 he moved to Nanjing Tech University. He has published over 350 papers in peer-reviewed journals with H-index > 80, was named in the World's Most Influential Minds (2015) list by Thomson Reuters, won the Albert Nelson Marquis Lifetime Achievement Award (2019), and was listed as one of the Highly Cited Researchers all over the world. He conducted pioneering research work on ARLBs, gel-type and pore-free separators for lithium batteries with high safety, and nitrogen fixation.

1 Introduction

Against the background of increasing population and global energy consumption connected with burning fossil fuels and worldwide environmental issues, creating an energy system based on efficient, clean and sustainable resources is particularly significant to secure our energy supply.[1,2] Ammonia (NH_3) as one of the most widely produced industrial chemicals has found wide applications in the manufacture of fertilizers (at least 80% of total ammonia annually) and pharmaceuticals, as well as energy conversion.[3] Particularly, compared to other energy carriers, NH_3 is recognized as an ideal storage medium for hydrogen (H_2), because it has a relatively high hydrogen content (17.6% by mass) and can exist easily in liquid form.[4–8] Besides, nitrogen is an indispensable element of life and a crucial component of various bio-macromolecules (amino acids, nucleotides and the like). However, since the N≡N triple bond has a high bond energy of 945 kJ mol^{-1} at 298 K, it is difficult to crack and hydrogenate.[9] Even though the atmospheric nitrogen (N_2) content is 78%, organisms normally obtain N in the form of NH_3 or nitrate (NO_3^-) instead of directly using N_2 molecules. In nature, NH_3 can be obtained by fixing N_2 either by lightning or through the action of microbial nitrogenases.[10] Generally, bacteria of the genus *Azotobacter* use adenosine triphosphate (ATP) as an energy transporter, and an iron–molybdenum–sulphur (FeMoS) core cluster as the main N_2 binding site to achieve the conversion of N_2 into NH_3 through migrating

© 2021 The Author(s). Published by the Royal Society of Chemistry

Open Access Article. Published on 13 1400. Downloaded on 14/02/1405 07:56:34 ..
This article is licensed under a Creative Commons Attribution-NonCommercial 3.0 Unported Licence.

multiple protons and electrons under ambient conditions.[11–13] However, microorganisms containing nitrogenase in nature alone cannot sufficiently match the demand for fertilizer use. Industrially, the Haber–Bosch process with Fe-based[14,15] or Ru-based[16,17] catalysts has been the main NH_3 production method over the last 100 years, and is operated under harsh conditions (around 400 °C, 50 bar), thus suffering from high energy consumption and severe equipment requirements.[18,19] In addition, H_2 is generally produced by the steam reformation of CH_4, which also depletes fossil fuels immensely and causes excessive CO_2 emissions. The social cost of CO_2 emissions and the impact of global fuel prices on geopolitics also limit the long-term development of conventional NH_3 processes.[20] Therefore, NH_3 synthesized from water and atmospheric N_2 using electric power is a promising method to convert unstably stored electricity into chemical energy. Moreover, feedstocks like water and N_2 are abundant and eco-friendly, acting as a proton source and N source, respectively. Since Davy's group developed the N_2 reduction reaction (NRR) method in 1807, researchers around the world have used various catalysts with different structures and compositions to activate N_2.[21] Attracted by the attention of various countries and the huge prospects of electrocatalysis, the NRR field has developed tremendously over the past five years (Fig. 1a). So far, various active centre nanomaterials such as precious metals (Au, Ag, Ru, Pd, *etc.*), non-precious metals (Fe, Mo, Co, Ti, *etc.*), and metal-free (B, C, *etc.*) (Fig. 1c) have been investigated to match some suitable low-dimensional substrates to improve the catalytic performance of NH_3 yield and faradaic efficiency (FE). However, in some representative studies (Fig. 1b), around 70% of the catalysts appear in the low performance zone of low NH_3 yield

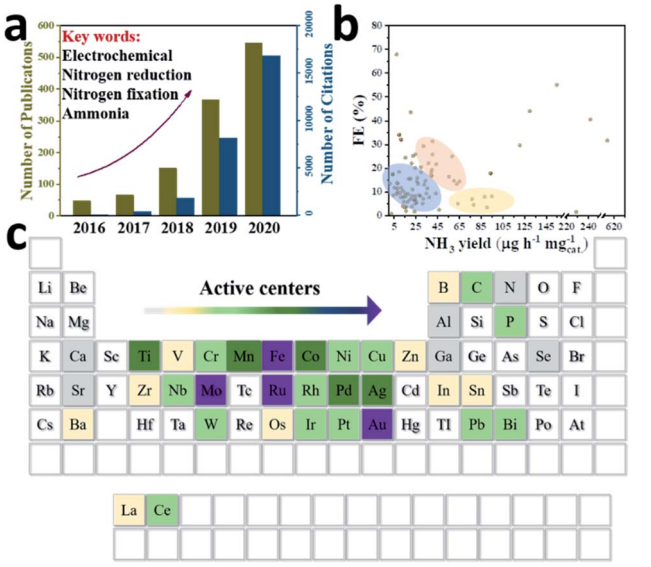

Fig. 1 (a) The number of publications and citations of NRR articles in the Web of Science in the last 5 years. (b) Reported NH_3 yield rate and FE of some representative articles. (c) The types of NRR electrocatalyst active centre published to date. The direction of the arrow represents the number of reports.

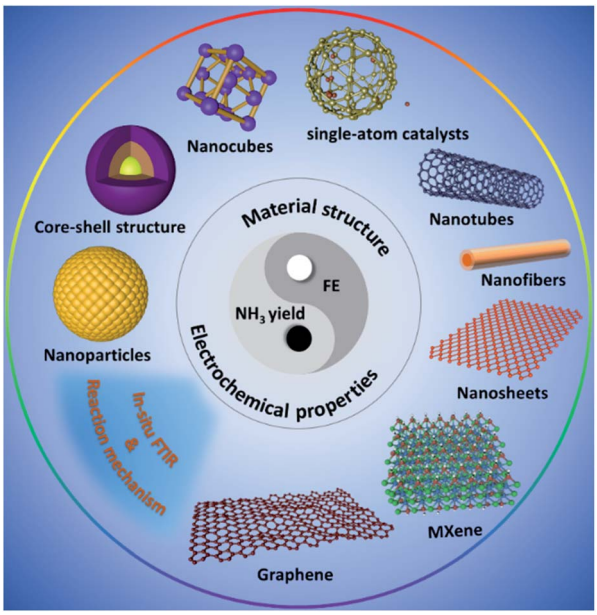

Fig. 2 Schematic overview of the NRR materials covered in this section.

or low FE, which is not conducive to the industrialization of the production process. According to S. Giddey's suggestion, the commercial process needs to achieve an NH_3 yield of 6.5 $\times 10^{-7}$ mol cm^{-2} s^{-1} or 3978 μg $mg_{cat.}^{-1}$ h^{-1} (mass loading: 0.1 mg cm^{-1}), and a FE of about 50%, with a current density above 0.25 A cm^{-2}.[22] Therefore, these issues should be solved before attempting to produce NH_3 on a large scale: firstly, the N≡N bond is hard to activate – the high N≡N bond energy makes it difficult for the N_2 activation reaction to proceed. Therefore, some key strategies to improve the kinetics of the NRR need to be developed. Secondly, the competing hydrogen evolution reaction (HER) should be considered. Since the NRR and HER have similar reaction potentials, choosing a catalyst with high selectivity that can inhibit the HER is the key to finding an efficient and sustainable NH_3 synthesis route.[23] Moreover, a rational material morphology should be designed because of the significant difference in the reaction rates of materials on different exposed surfaces with different morphologies. Therefore, it is necessary to design a series of advanced catalysts to realize revolutionary progress in the NRR field.

In this review, we will mainly summarize the recent progress of some advanced low-dimensional nanomaterials in N_2 fixation under ambient conditions from experimental and theoretical perspectives, aiming at inspiring new perceptions for the future in this field. Firstly, we discuss the NRR mechanisms, reaction intermediates and credibility studies of the NRR. Then, we summarize some typical low-dimensional nanomaterials, discussing the relationship between the structure and NRR performance from both the theoretical and experimental perspectives. Finally, we provide some insights into the development of NRR electrocatalysts from the perspective of electronic control.

© 2021 The Author(s). Published by the Royal Society of Chemistry

Open Access Article. Published on 13 1400. Downloaded on 14/02/1405 07:56:34 ..
This article is licensed under a Creative Commons Attribution-NonCommercial 3.0 Unported Licence.

2 Reaction mechanisms

2.1 Theoretical basis

The electrochemical NRR is generally completed in an H-type cell. The overall reaction equation is shown in eqn (1):

$$N_2 + H_2O \rightarrow NH_3 + O_2 \quad (1)$$

The anodic reaction is shown in eqn (2) and (3):

$$\text{Acidic electrolyte: } 3H_2O \rightarrow 3/2O_2 + 6H^+ + 6e^- \quad (2)$$

Alkaline or neutral electrolyte:

$$6OH^- \rightarrow 3/2O_2 + 3H_2O + 6e^- \quad (3)$$

The cathodic reaction is shown in eqn (4) and (5):

$$\text{Acidic electrolyte: } N_2 + 6H^+ + 6e^- \rightarrow 2NH_3 \quad (4)$$

Alkaline or neutral electrolyte:

$$N_2 + 6H_2O + 6e^- \rightarrow 2NH_3 + 6OH^- \quad (5)$$

The first important step of the NRR is the adsorption and activation of N_2, which is highly related to the electronic state of the electrocatalyst. For the ground state of N_2, the bonding HOMO is $3\sigma_g$, and the antibonding LUMO is $1\pi_g^*$. Taking transition metals as an example, N_2 donates electrons to the empty d orbital from its HOMO and accepts electrons to its LUMO, thereby being adsorbed on the catalyst and forming bonds.[24] This electron donation and acceptance process is beneficial to adsorbing N_2 and weakening the N≡N bonds.[25] The NRR is accompanied by a series of hydrogenation steps, including the breaking of N≡N bonds and the formation of N–H bonds. Generally speaking, N_2 hydrogenation has two main mechanisms, the dissociative mechanism and the associative mechanism (Fig. 3).[26,27] In the dissociative mechanism, the N≡N bond is broken before hydrogenation. Then, each N atom is hydrogenated separately until two NH_3 molecules are formed. This approach requires a high activation energy to overcome the high energy barrier during the direct cleavage of N≡N bonds. In the associative mechanism, one N atom in the N_2 molecule is first adsorbed on the surface of the electrocatalyst, and then gradually hydrogenated. Generally, the mainstream pathways in the associative mechanism for converting N_2 to NH_3 can be classified into two hydrogenation routes, distal hydrogenation and alternating hydrogenation. In the distal hydrogenation path, H is added one by one to the N atom farthest away from the catalyst surface. When this N atom is converted to NH_3, the N–N bond is broken. Then, the other N atom adsorbed on the surface of the catalyst is converted into NH_3 in the same way. In the alternating hydrogenation route, hydrogenation occurs alternately on the two N atoms. After the first N atom is converted to NH_3, the remaining $-NH_2$ will absorb another proton to form a second NH_3 molecule. The enzymatic pathways belonging to the associative pathway exhibit the unique characteristics of lateral adsorption, rather than terminal adsorption in the alternating and distal pathways. The current research work shows that the N_2 fixation in the Haber–Bosch process is mainly caused by the dissociative

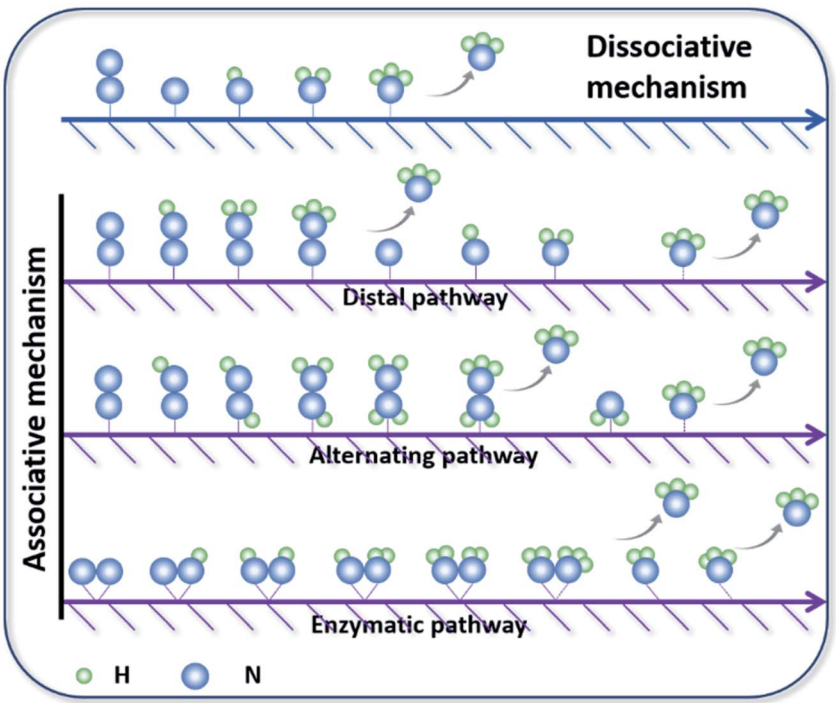

Fig. 3 Mainstream mechanisms for N_2 reduction to NH_3 on catalysts. Copyright 2016, Elsevier B.V.[26] Copyright 2016, American Chemical Society.[27]

Open Access Article. Published on 13 1400. Downloaded on 14/02/1405 07:56:34 ..
This article is licensed under a Creative Commons Attribution-NonCommercial 3.0 Unported Licence.

mechanism.[28] Therefore, high-temperature and high-pressure reaction conditions are necessary for the cleavage of N≡N bonds. However, cleavage of the N≡N bond in the associative mechanism is not necessary, which significantly reduces the energy input during the N_2 activation process, allowing the reaction to proceed under relatively mild conditions. Therefore, the separate or mixed partial radical steps of the distal, alternating, and enzymatic pathways dominate in the NRR.

2.2 Research on intermediate products

Although it is important to determine the NRR mechanism to further improve the absorbance and activation of N_2 on the surface of the catalyst, few experimental studies have been published on the significant effects of the NRR. *In situ* Fourier transform infrared spectroscopy (*in situ* FTIR) technology based on electrochemistry has become a new method to explore the N_2 reduction pathways, employed to detect the change of functional groups (like *NNH, *HNH, and *NH_3) on the electrocatalyst surface during the NRR. By using *in situ* FTIR, key information about the real-time adsorption state of reactants and the structural transformation of intermediates on the catalyst surface could be obtained during the reaction process.[29] Shao's group investigated the composition and content of Pt and Au surface functional groups at different potentials by surface-enhanced infrared absorption spectroscopy (SEIRAS).[30] Fig. 4a shows the change in functional groups at the Au surface in N_2-saturated solution under the first CV segment. It can be seen clearly that the intensity of δ(H–N–H) and δ(N–N) gradually increases as the potential grows more negative in the N_2-saturated solution. At the Pt surface, the characteristic peaks between 1300 and 1500 cm^{-1} are not observed (Fig. 4b), due to the much faster kinetics of the HER. Based on this analysis, it was believed that there was an associative reaction mechanism on the Au surfaces. Furthermore, they deduced a new possible NRR pathway on Rh surfaces by SEIRAS and differential electrochemical mass spectrometry (DEMS), that is, first reduction to N_2H_2 on the Rh surface, and then chemical dissociation in the electrolyte to form NH_3.[31] The optimal potential and materials have also been analysed by Yan.[32] Combining LSV (Fig. 4c), *in situ* FTIR (Fig. 4d) and *in situ* Raman (Fig. 4e), they studied the catalyst reaction interface. Compared to the BCP (left) and PVDF@BCP (right), the *in situ* FTIR (Fig. 4d) of ECOF@BCP (middle) additionally displayed obvious ν(N–H) with increasing intensity as the potential became more negative, which is consistent with LSV. According to the position of the cathodic peak in the LSV, the potential of −0.3 V *vs.* RHE was selected for *in situ* Raman spectroscopy. Fig. 4e shows the gradual formation of NH_3 on the surface of ECOF@BCP.

2.3 Credibility studies

The fundamental problem with the NRR is that the amount of NH_3 produced is very small, yet NH_3 is a common contaminant in the laboratory environment, which has led to a large number of rigorous experiments being carried out to verify the reliability of the NRR activity of the material. The reasons for the discrepancies in the experimental data can be broadly classified as follows: contamination of the raw material (water, catalyst, catalyst carrier, electrolyte, and feed gas), air contamination, deterioration of the colour developer and decomposition of the catalyst. For feedstock contamination, eight sets of comparison

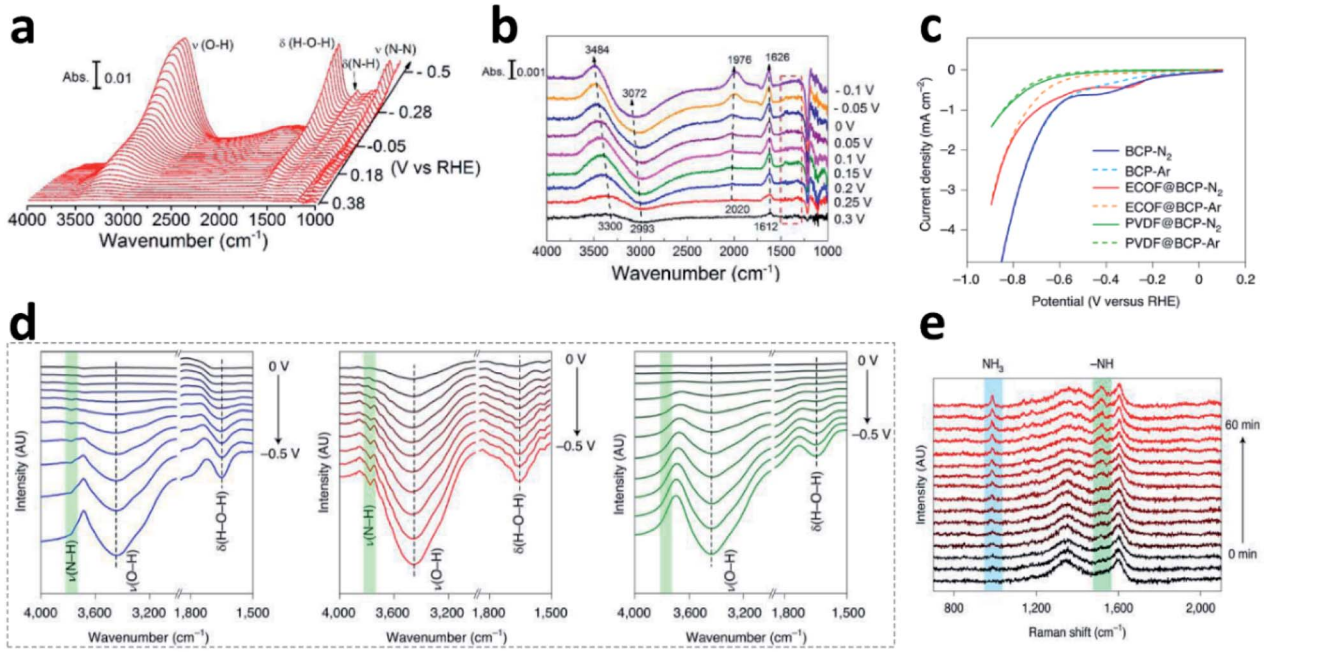

Fig. 4 FTIR spectra during the CV on the Au (a)/Pt (b) film in N_2-saturated solution. Copyright 2018, American Chemical Society.[30] (c) LSV of different electrodes in feed gas. (d) *In situ* FTIR spectra of BCP (left), ECOF@BCP (middle) and PVDF@BCP (right) under feed gas. (e) *In situ* Raman spectra of ECOF@BCP at −0.3 V *vs.* RHE. Copyright 2021, Springer Nature.[32]

© 2021 The Author(s). Published by the Royal Society of Chemistry

Open Access Article. Published on 13 1400. Downloaded on 14/02/1405 07:56:34 ..
This article is licensed under a Creative Commons Attribution-NonCommercial 3.0 Unported Licence.

experiments using the controlled variable method for NRR systems can be verified: (1) non-catalyst-Ar-open circuit voltage (OCV), (2) non-catalyst-N_2-OCV, (3) non-catalyst-Ar-working voltage (WV), (4) non-catalyst-N_2-WV, (5) catalyst-Ar-OCV, (6) catalyst-N_2-WV, (7) catalyst-Ar-WV, (8) catalyst-N_2-WV. For air contamination, the same volume of electrolyte placed daily on the operating table allows for monitoring of NH_3 contamination in the laboratory. For colour reagent deterioration, the standard curve should be calibrated weekly and all batches of electrolyte are coloured for the same time. For catalysts containing N, ^{15}N NMR is necessary to ensure that the source of NH_3 is N_2 and not the decomposition of the catalyst.

3 Nanomaterial NRR electrocatalysts

For electrocatalytic N_2 fixation, nanomaterials have a uniform exposed lattice and can realize more exposed active sites under a certain mass loading compared with conventional bulk catalysts. Nanomaterials encompass a broad spectrum of tunable physical and chemical properties including a high surface to volume ratio and abundant active sites, making them immensely useful for a wide range of catalytic reactions. Low-dimensional nanocatalysts are highly designable because their surface structures and electronic properties are very sensitive to particle size and morphology. In this section, we will briefly summarize the synthetic methods and corresponding unique properties of these advanced nanomaterials, which are grouped into four categories based on material morphology (Fig. 2): zero-dimensional (0D) nanomaterials, including nanoparticles (NPs), nanospheres, quantum dots (QDs) and single-atom catalysts (SACs); one-dimensional (1D) nanomaterials such as nanofibers (NFs), nanowires (NWs), nanorods (NRs), and nanotubes (NTs); and two-dimensional (2D) nanomaterials such as nanosheets (NSs), graphene (G), C_3N_4, MXene, and other non-layered carbon compounds.

3.1 Zero-dimensional (0D) nanomaterials

0D nanomaterials have ultra-small sizes, high specific surface area and huge numbers of active edge sites. The most typical 0D materials are NPs, which can be crystalline or amorphous, monometallic, multicomponent, or metal-free materials. In catalysis, NPs are the most common nanomaterials due to the relatively easier synthetic procedures. Over the past few decades, a rich variety of chemical methods (like chemical exfoliation, sonication-assisted exfoliation, chemical vapor deposition (CVD), solvothermal processing, cautery technique, and laser ablation technique) have been developed to fabricate 0D NPs with well-controlled sizes and shapes.[33] In this section, we will briefly review the synthetic strategies for various 0D NRR catalysts. The performance of some 0D electrocatalysts is summarized in Table 1.

The NPs were fabricated applying a series of solvothermal strategies using various precursors. The general approach for preparing NPs is using a solvothermal process to prepare precursors followed by annealing treatment, or using sacrificial templates. Some pioneering researches on TiO_2 as the NRR nanocatalyst were done by Sun's group.[54,55] They fabricated C-doped TiO_2 NPs by dispersing titanium butoxide in water/ethanol (5 : 30) solution, followed by hydrothermal and annealing treatment. A yield of 16.22 $\mu g\ h^{-1}\ mg_{cat.}^{-1}$ NH_3 was obtained with a 1.84% FE at −0.7 V *vs.* RHE in Na_2SO_4. However, the amorphous carbon may cover the active sites of the catalyst during the synthesis process, resulting in a relatively low yield of NH_3. Therefore, modulating the vacancy concentration and defect states may increase the active site density effectively.

Table 1 Summary of 0D nanomaterials for the NRR

Catalyst[ref.]	Electrolyte	NH_3 yield ($\mu g\ h^{-1}\ mg_{cat.}^{-1}$)	NH_3 yield ($\times10^{-10}$ mol s^{-1} cm^{-2})	FE (%)	Potential (V *vs.* RHE)
MV-MoN@NC[34]	0.1 M HCl	≈76.90		6.90	−0.20
AuCu/ZIF-8 (ref. 35)	0.1 M HCl	63.90	—	5.00	−0.20
Pt/Au@ZIF[36]	THF + CF_3LIO_3S + 1% ethanol	>130	—	44.00	—
Au NPs[37]	0.1 M Na_2SO_4	17.49	—	5.79	−0.14
Au_1Cu_1 (ref. 38)	0.05 M H_2SO_4	154.91	—	54.96	−0.2
$Fe_2(MoO_4)_3$ (ref. 39)	0.1 M Na_2SO_4	18.16	—	9.10	−0.60
Mn_3O_4 NPs[40]	0.1 M Na_2SO_4	25.95	—	5.51	−0.50
ZrO_2 NPs[41]	0.1 M HCl	24.74	—	5.00	−0.45
C/Y stabilized ZrO_2 (ref. 42)	0.1 M Na_2SO_4	24.60	—	8.20	−0.50
np-$PdH_{0.43}$ (ref. 43)	0.1 M PBS	20.40	—	43.60	−0.15
Body-centered cubic PdCu NPs[44]	LiCl	35.70	—	11.50	−0.10
B and N dual-doped C nanospheres[45]	0.05 M H_2SO_4	15.70	—	8.10	−0.04
Defect-rich MoS_2 nanoflowers[46]	0.1 M Na_2SO_4	29.28	—	8.34	−0.40
BP QDs/MnO_2 (ref. 47)	0.1 M Na_2SO_4	25.30	—	6.70	−0.50
BP QDs@SnO_{2-x} (ref. 48)	0.1 M Na_2SO_4	29.22	—	18.00	−0.40
Ru SAs/N–C[49]	0.05 M H_2SO_4	120.90	—	29.60	−0.20
Fe-$(O–C_2)_4$ (ref. 50)	0.1 M KOH	32.10	—	29.30	−0.10
SACs-MoS_2-Fe[51]	0.1 M KCl	613.70	15.93	31.60	−0.20
Ni_x-N-C-700-3h[52]	0.5 M Li_2SO_4	—	18.79	21.00	—
SA-Mo/NPC[53]	0.1 M KOH	34.00	—	14.60	−0.30

Open Access Article. Published on 13 1400. Downloaded on 14/02/1405 07:56:34 ..
This article is licensed under a Creative Commons Attribution-NonCommercial 3.0 Unported Licence.

Recently, Cu ions with mixed valences of +1 and +2 were also introduced into TiO_2 NPs by hydrothermal reaction to modulate the oxygen vacancy concentration and Ti^{3+} defect states (Fig. 5a).[55] Due to the chemical compensation effect, mixed-valent Cu can induce different electronic defect states in TiO_2, thereby spontaneously adjusting the oxygen vacancies (OVs) concentration. Introduction of mixed valence Cu modulates the surface of TiO_2 (101) to generate OVs with different Ti^{3+} $3d^1$ defect states below the Fermi energy. By adjusting the coordination structure, the activation and adsorption of N_2 can be enhanced effectively. Moreover, the catalytic performance is related to both Ti^{3+} and Cu contents. When the content of Cu was 6.9%, the Cu-doped TiO_2 NPs attained a high FE of 21.99% with 21.31 $\mu g\ h^{-1}\ mg_{cat.}^{-1}$ NH_3 yield at −0.55 V *vs.* RHE in 0.5 M $LiClO_4$. Indeed, semiconductor materials with OVs can contribute to a certain NRR activity.[56] If combined with other NRR active components like noble Au, the catalytic performance may also improve synergistically. Due to the easy Ce^{3+}/Ce^{4+} redox cycle and abundant OVs, CeO_2 has been widely investigated as a catalyst.[57] Zhang's group reported a core–shell structure Au@CeO_2 with a small core layer of Au NPs (<10 nm).[58] The combination of abundant OVs in the shell layer of CeO_2 NPs and small-sized Au NPs in the core layer enhances the NRR performance synergistically. The same group also developed core–shell Au/C NPs (Fig. 5b) by laser ablation, which consists of a spherical Au core and 1–2-layer graphite carbon shell with a large number of defects.[59] The ultrathin carbon layer inhibits the aggregation of Au nanospheres effectively during the electrochemical reaction. Alternatively, there are a large number of carbon vacancies in the ultrathin carbon layer, which can provide additional catalytically active sites for the NRR. Hence, the core–shell Au/C NPs can afford an excellent performance (NH_3: 241.9 $\mu g\ h^{-1}\ mg_{cat.}^{-1}$, FE: 40.5%) at −0.45 V *vs.* RHE in neutral solution. Apparently, the synergistic effect between the carbon vacancies in the ultrathin graphitic carbon layer and the inner active Au nanospheres enhanced the NRR activity.

To utilize Au effectively, Jiang's group embedded Au sub-nanoclusters onto the TiO_2 surface and stabilized them with lattice oxygen to form Au–O–Ti bonds. The positively charged Au centre in the Au–O–Ti bond is the active site for forming the chemically adsorbed Au–N_2 bond. These small Au sub-nanoclusters (≈0.5 nm) with few coordination sites as isolated precious metal active centres dispersed on the TiO_2 support lead to effective and stable NRR performance (Fig. 5c).[60] Xue and co-workers constructed inorganic donor−acceptor metal couples to increase electron density.[61] The highly coupled Au_6/Ni NPs exhibited a high FE of 67.8% at −0.14 V *vs.* RHE. The author suggested that Ni provides numerous electrons for Au, which boosts the NRR activity of electron-rich Au. DFT calculations further proved that both the Gibbs free energy (ΔG) of N_2 dissociation and the desorption energy of NH_3 molecules on the electron-rich Au surface were reduced (Fig. 5d and e). Quantum

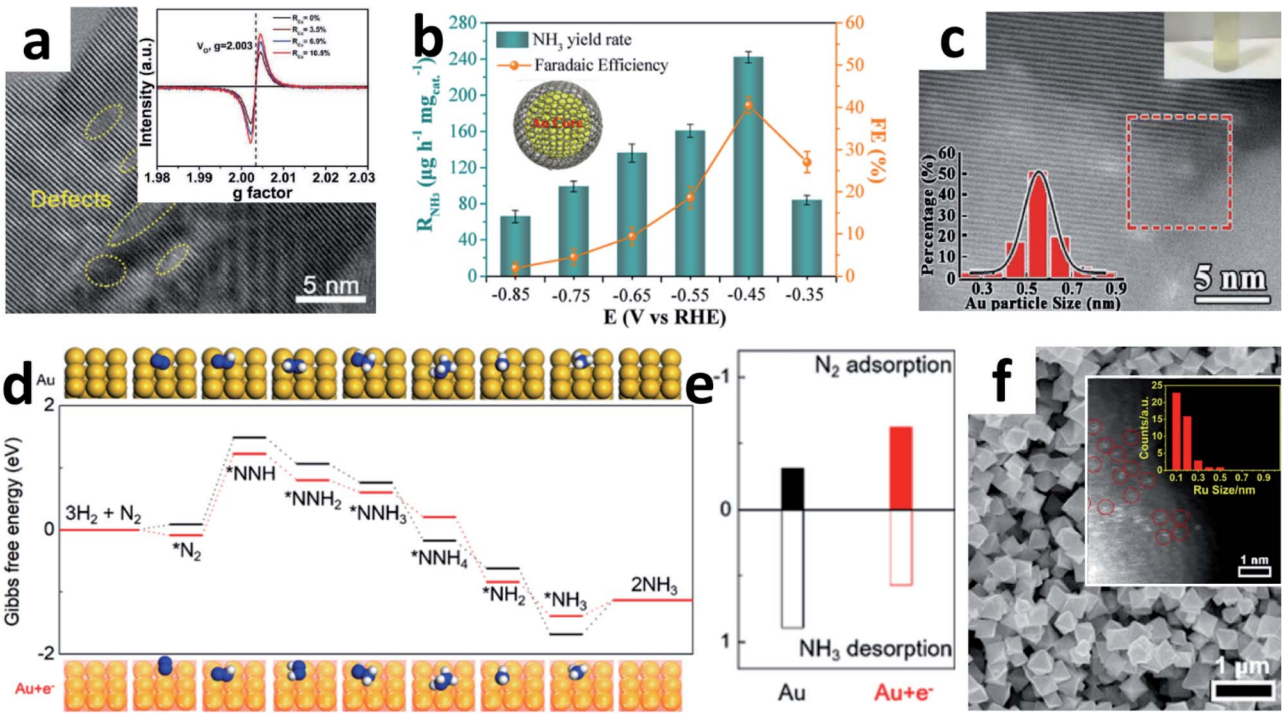

Fig. 5 (a) HRTEM image of Cu–TiO_2 NPs (inset: EPR spectra of Cu–TiO_2 with different Cu contents). Copyright 2020, Wiley-VCH.[55] (b) Performance of Au@C at different applied potentials (inset: the structural diagram of Au@C). Copyright 2019, American Chemical Society.[59] (c) HAADF-STEM image of the TA-reduced Au/TiO_2 (top inset: the photograph of the catalyst suspended in water; bottom inset: Au particle size distribution). Copyright 2017, Wiley-VCH.[60] (d) Gibbs free energy diagram of the NRR for Au and Au + e^- (insets: the corresponding optimized adsorption structures). (e) The calculated adsorption energies and desorption energies for adsorption onto Au and Au + e^-.[61] (f) SEM image of Ru@ZrO_2/NC (inset: the size-distribution histogram of Ru). Copyright 2019, Elsevier Inc.[69]

© 2021 The Author(s). Published by the Royal Society of Chemistry

Open Access Article. Published on 13 1400. Downloaded on 14/02/1405 07:56:34 ..
This article is licensed under a Creative Commons Attribution-NonCommercial 3.0 Unported Licence.

dots (QDs) are nanoclusters that behave like atoms, which can significantly affect the chemical and physical properties of nanomaterials. Taking BP QDs as an example, the ultrafine BP QDs anchored on either MnO_2 NSs[47] or SnO_{2-x} NTs[48] could synergistically promote the NRR. Shao's group developed a 1T-MoS_2/g-C_3N_4 with ultra-small sized MoS_2 QDs for the NRR.[62] The metallic 1T-MoS_2 nanodots anchored on g-C_3N_4 NSs have abundant active sites and excellent conductivity, thereby achieving a comparable FE of 20.48% under demanding HER conditions.

Single-atom catalysts (SACs) are the ultimate form of 0D NPs, where all the atoms are surface active sites. Due to the homogeneity of the catalytically active sites, low coordination environment and maximal utilization efficiency, SACs have high catalytic activity, stability and selectivity for a series of electrochemical processes.[63–66] Some reports have explored the application of SACs anchored on N-doped porous carbon for the NRR.[53,67,68] In 2018, Zeng's group prepared single Ru atoms distributed on N-doped C by pyrolyzing a Ru-containing derivative of ZIF-8.[49] The isolated Ru atom was dispersed on the whole Ru SAs/N–C and without Ru–Ru bond contribution. The Ru SAs/N–C reached a high NH_3 production rate (120.9 μg h^{-1} $mg_{cat.}{}^{-1}$) and FE (29.6%) at −0.2 V *vs.* RHE. In particular, the FE of Ru SAs/N–C was 2.1 times higher than that of Ru NPs/N–C. Reducing the size of Ru particles to the atomic level should obviously improve efficiency. In addition, Tao *et al.* developed a thermal pyrolysis method anchoring single Ru atoms onto a Zr-based MOF to suppress the HER.[69] They claimed that control of the Ru size by the choice of ligand and the inhibitory effect of ZrO_2 on the HER facilitate the dissociation of N_2. DFT also showed that the Ru sites with OVs were major active centres for enhancing N_2 fixation. Due to these remarkable properties, the Ru@ZrO_2/NC catalysts (Fig. 5f) achieved a significant NH_3 production rate of 3.665 mg h^{-1} $mg_{Ru}{}^{-1}$ at −0.21 V *vs.* RHE. Moreover, the FEs of Ru@ZrO_2/C and Ru@ZrO_2/NC were significantly higher than those of Ru/C and Ru/NC, indicating that ZrO_2 could probably suppress the HER during the NRR.

3.2 One-dimensional (1D) nanomaterials

As an emerging class of nanomaterials, 1D materials exhibit excellent catalytic activity due to their fast charge transport, large active surface area and rapid mass transport.[70–72] Compared with their bulk, 0D and 2D counterparts, the 1D structure has the following characteristics: first, the diameter of the material is limited to the nanoscale, so it shows high atom efficiency while preserving the relatively stable structure. Then, the large number of open spaces between adjacent 1D nanostructures facilitate both chemical accessibility and mass transport of electrolyte deep into the electrode.[73] Moreover, for electrocatalysis, the surface of the 1D nanomaterials can greatly facilitate the formation and release of bubbles, thus preventing them from occupying the active sites and hindering subsequent reactions.[74–76] The synthetic methods for 1D nanomaterials include electrospinning, electrodeposition, solvothermal reactions, template-assisted methods, and mediated growth.[70,71] Thus, advanced 1D nanomaterials including NFs, NWs, NTs and NRs will be briefly reviewed in this section. The performance of some 1D electrocatalysts is summarized in Table 2.

The electrospinning method is one of the most convenient methods for constructing complex 1D nanomaterials. Up to now, various 1D NWs and NTs have been synthesized by a spinneret electrospinning process for research on batteries and electrocatalysis.[70,91] Yu's group designed an amorphous $Bi_4V_2O_{11}$/CeO_2 hybrid obtained by electrospinning.[88] The OVs and defective sites in $Bi_4V_2O_{11}$/CeO_2 are able to trap electrons in the metastable state, so that the electrons are injected into the antibonding orbital of the adsorbed N_2, thereby weakening the N≡N triple bond and promoting catalytic activity. Similarly, Sun's group also reported a novel metal oxide synthesized by this method.[77] The Nb_2O_5 NFs were shown to be a superior NRR catalyst with a high NH_3 yield (43.60 μg h^{-1} $mg_{cat.}{}^{-1}$ at −0.55 V *vs.* RHE) and FE (9.26%). DFT calculations show that the electrocatalytic reaction takes place on the active sites on the surface (181), and the key energy barrier could be eliminated by applying a potential of −0.56 V. The same group also reported the Ti^{3+} self-doped TiO_{2-x}

Table 2 Summary of 1D nanomaterials for the NRR

Catalyst[ref.]	Electrolyte	NH_3 yield (μg h^{-1} $mg_{cat.}{}^{-1}$)	NH_3 yield ($\times10^{-10}$ mol s^{-1} cm^{-2})	FE (%)	Potential (V *vs.* RHE)
Nb_2O_5 NF[77]	0.1 M HCl	43.6	—	9.26	−0.55
AuPdP NWs[78]	0.1 M Na_2SO_4	18.78	1.23	15.44	−0.30
CBC/V_r-$ReSe_2$@CBC/CBC[79]	0.1 M Na_2SO_4	—	4.62	42.5	−0.25
Ti^{3+} self-doped TiO_{2-x} NWs[80]	0.1 M Na_2SO_4	—	0.35	14.62	−0.55
C@CoS@TiO_2 NFs[81]	0.1 M Na_2SO_4	—	8.09	28.60	−0.55
Fe-doped $W_{18}O_{49}$ NWs[82]	0.25 M $LiClO_4$	24.70	—	20.0	−0.15
Fe–MnO_2 (ref. 83)	0.1 M Na_2SO_4	39.20	—	16.80	−0.29
α-Fe_2O_3@mTiO_2 (ref. 84)	0.1 M Na_2SO_4	27.20	—	13.30	−0.50
Fe–N/C-CNTs[85]	0.1 M KOH	34.83	—	9.28	−0.20
CoVP@NiFeV-LDH HHNTs[86]	0.05 M H_2SO_4	—	4.44	13.80	−0.30
Mo_2C NRs[87]	0.1 M HCl	95.10	—	8.13	−0.30
Bi_4O_{11}/CeO_2 (ref. 88)	0.1 M HCl	23.21	—	10.16	−0.20
CNT@C_3N_4–Fe & Cu[89]	0.25 M $LiClO_4$	9.86	—	34.00 (−0.80 V)	−1.20
Surface-rough Rh_2Sb NRs[75]	0.5 M Na_2SO_4	228.85	—	1.50	−0.45
IrP_2@PNPC-NF[90]	0.05 M H_2SO_4	94.00	—	17.80	−0.20

© 2021 The Author(s). Published by the Royal Society of Chemistry

Open Access Article. Published on 13 1400. Downloaded on 14/02/1405 07:56:34 ..
This article is licensed under a Creative Commons Attribution-NonCommercial 3.0 Unported Licence.

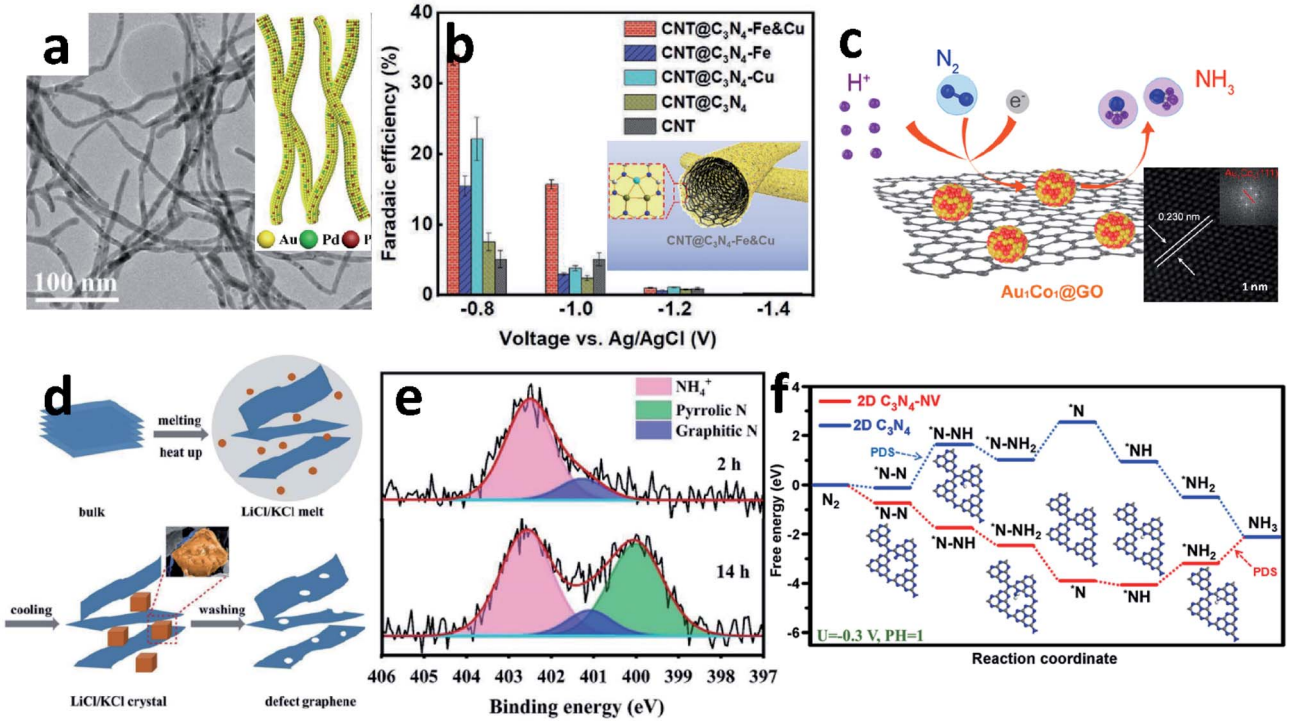

Fig. 6 (a) TEM image of AuPdP NWs (inset: schematic diagram of AuPdP NWs). Copyright 2019, American Chemical Society.[78] (b) The FE of different materials at different potentials (inset: schematic diagram of CNT@C_3N_4-Fe & Cu). Copyright 2020, Wiley-VCH.[89] (c) Schematic diagram of the NRR of Au_1Co_1@GO (inset: HRTEM image of Au_1Co_1@GO). Copyright 2019, American Chemical Society.[117] (d) Schematic diagram of defect graphene (DG) synthesis. (e) N 1s spectra of DG-800 after reaction. Copyright 2020, The Royal Society of Chemistry.[131] (f) Gibbs free energy of C_3N_4 and C_3N_4-NV for the NRR. Copyright 2021, Elsevier B.V.[138]

NWs supported on Ti mesh.[80] Introducing Ti^{3+} into the TiO_2 surface could decrease the energy barrier of electron transfer and increase the number of active sites to obtain a higher NH_3 yield (3.51×10^{-11} mol s^{-1} cm^{-2}) with 14.62% FE at −0.55 V *vs.* RHE, compared to TiO_2/TM (1.89×10^{-11} mol s^{-1} cm^{-2}, 6.49%). Wang *et al.* synthesized AuPdP NWs by simultaneously incorporating Pd and P into a controlled morphology Au particle (Fig. 6a).[78] There is a strong interaction between Au, Pd and P in the NWs. Pd, which has a stronger adsorption effect on H, improves the H adsorption on the Au surface;[92] and the incorporation of P provides more valence electrons, which is beneficial to the selective hydrogenation of N_2 to NH_3. Thus, AuPdP NWs achieved an NH_3 yield of 18.78 μg h^{-1} $mg_{cat.}^{-1}$ and FE of 15.44% at −0.3 V *vs.* RHE. Although defect engineering has been repeatedly proven as a rational strategy to enhance electrocatalytic performance, it has poor selectivity between the NRR and HER. The side-effects of the HER mean that the NRR is still far from commercialization. Recently, Liu *et al.* reported a novel "sandwich" structure, CBC/Vr-$ReSe_2$@CBC/CBC (CBC = carbonized bacterial cellulose, Vr-$ReSe_2$ = vacancy-rich $ReSe_2$).[79] The surface of the hydrophobic CBC layer resists the intimate contact between water molecules and Vr-$ReSe_2$@CBC NFs, and slightly increases the adhesive force to N_2 bubbles, so the FE is boosted by 32% at −0.25 V *vs.* RHE compared with Vr-$ReSe_2$@CBC without the CBC sandwich structure.

NRs are the most common 1D morphology because they contain exposed stepped faces, remarkably boosting their catalytic performance.[93–96] In 2017, Ren *et al.* demonstrated Mo_2N NRs as an efficient NRR electrocatalyst.[97] According to the DFT calculations, after nitrogenation, the ΔG of the potential determining step of the NRR on MoO_2 decreased dramatically. Later, this group developed MoC NRs based on Mo_2N, which was synthesized by pyrolyzing a $Mo_3O_{10}(C_6H_8N)_2 \cdot 2H_2O$ precursor in an Ar atmosphere. The FE of MoC is 1.8-fold that of Mo_2N.[87] Porous $FeVO_4$ NRs have been reported as an effective NRR catalyst contributing to the dual active centres.[98] The dual active centres of the Fe_{2c}-V_{2c} dimer can jointly back-donate their 3d-electrons into the antibonding $1\pi_g^*$ orbital of $*N_2$, and this process strongly polarizes and activates N_2, increasing the NH_3 yield up to 52.8 μg h^{-1} mg^{-1}. Moreover, coordination of Fe and Cu also enhanced the NRR. From Chu's report, the ordered sub-nano space in the surface cavities of CNT@g-C_3N_4 can accommodate several Fe and Cu atoms, forming a sub-nano reactor with tight coordination between Fe and Cu.[89] Compared to their single-metal counterparts, the coordination between Cu and Fe can accelerate the adsorption of N_2 synergistically to optimize the reaction path and lower the energy barrier, thereby improving the FE to up to 34% (Fig. 6b).

3.3 Two-dimensional (2D) nanomaterials

2D materials have a single and fully exposed crystal surface and unique electronic state, arousing enormous interest over a wide field of energy and storage.[99,100] Compared with their bulk, 0D

© 2021 The Author(s). Published by the Royal Society of Chemistry

Open Access Article. Published on 13 1400. Downloaded on 14/02/1405 07:56:34 ..
This article is licensed under a Creative Commons Attribution-NonCommercial 3.0 Unported Licence.

Table 3 Summary of 2D nanomaterials for the NRR

Catalyst[ref.]	Electrolyte	NH_3 yield ($\mu g\ h^{-1}\ mg_{cat.}^{-1}$)	NH_3 yield ($\times 10^{-10}$ mol $s^{-1}\ cm^{-2}$)	FE (%)	Potential (V *vs.* RHE)
Co-$FePS_3$ NSs[118]	0.1 M KOH	90.60	—	3.38	−0.40
Sn/SnS_2 (ref. 119)	0.1 M PBS	23.8	—	3.40	−0.80
B4C NSs[120]	0.1 M Na_2SO_4	26.57	—	15.95	−0.75
Bi NS[105]	0.1 M Na_2SO_4	13.23	0.42	10.46	−0.80
FeS_2-$Mo_{17.3}$ NSs[121]	0.1 M KOH	26.15	—	14.41	−0.20
Few-layer black phosphorus NSs[122]	0.01 M HCl	31.37	—	3.09	−0.70
Crystalline red phosphorus nanoribbons[109]	0.1 M Na_2SO_4	15.40	—	≈3.00	−0.40
IrP_2@PNPC nanofilm[90]	0.05 M H_2SO_4	94.00		≈10.00	−0.20
1T-MoS_2/g-C_3N_4 (ref. 62)	0.1 M HCl	29.97	—	20.48	−0.30
Hydroxyl-rich $Ti_3C_2T_x$ QDs[123]	0.1 M HCl	62.94	—	13.30	−0.50
Au/Ti_3C_2 (ref. 124)	0.1 M HCl	30.06	—	18.34	−0.20
Rh_2P@NPC[125]	0.1 M Na_2SO_4	37.60	—	7.64	−0.25
Au_1Co_1@GO[117]	0.5 M K_2SO_4	36.82	—	22.03	−0.20
CoO QD/RGO[111]	0.1 M Na_2SO_4	21.50	—	8.30	−0.60
CoS_2/NS-G[126]	0.05 M H_2SO_4	25.00	—	≈6.00	−0.20
rGO/Fe@Fe_3O_4/CP[127]	0.2 M $NaHCO_3$	—	1.30	6.25	−0.30
Boron-doped graphene (BG)[128]	0.05 M H_2SO_4	—	1.60	10.80	−0.50

and 1D counterparts, the 2D structure has the following characteristics: first, the 2D nanomaterials have exceptional flexibility and mechanical strength due to nanoscale thickness and strong in-plane covalent bonding. Then, thanks to their ultra-thin thickness and large transverse dimensions, 2D materials have a high specific surface area and surface atomic exposure. Moreover, for surfaces that expose a large number of atoms, researchers can design 2D nanomaterials for surface modification, elemental doping or vacancy engineering at the atomic level. Especially in recent years, various 2D nanomaterials (such as NSs, MXene, G, and C_3N_4) have been developed and utilized in the NRR electrocatalysis. The synthetic methods for 2D nanomaterials are mainly solvothermal reactions, CVD, template-assisted methods, topochemical transformations, salt-assisted synthesis, and self-assembly methods.[100–103] The performance of some 2D electrocatalysts is summarized in Table 3.

Nørskov *et al.* suggested using a less reactive main group element, semiconductor or thin insulator, to suppress the HER process and enhance the FE.[104] Qiao's group reported a semiconducting Bi NS with effective p-orbital electron delocalization and abundant exposure of edge sites, which exhibits a high NRR electrocatalytic activity.[105] Notably, materials with HER characteristics also promote the NRR. Wang's group developed ultrathin carbon NSs with Mo_2C DQs, which have high reactivity for both the NRR and HER.[106] Unlike the back-donation process of the transition metal complex, the B atoms have the characteristics of monovalent borylene, and the N_2 unit can be used as a Lewis s-donor and p-receptor.[107] In 2019, Zhang *et al.* developed a novel boron NS (BNS), whose B atoms were oxidized and H deactivated as a NRR electrocatalyst with an NH_3 production rate of 13.22 $\mu g\ h^{-1}\ mg_{cat.}^{-1}$.[108] Compared with traditional NSs, 2D nanoribbons have stronger size confinement effects. Recently, Liu *et al.* reported triclinic crystalline red phosphorus (cRP) nanoribbons as a large-scale synthetic nanocatalyst for the NRR in 0.1 M Na_2SO_4.[109]

As an ideal substrate to load electrocatalysts, graphene (G) has a large specific surface area and abundant material attachment sites, which can make the material grow evenly on the G surface to avoid agglomeration. Many G-based materials have been reported for the NRR.[110–114] Recent work by Chu *et al.* developed an advanced electrocatalyst, CuO/RGO, which was synthesized by a microwave-assisted solvothermal method.[115] The CuO/RGO exhibited a high NH_3 yield of 1.8×10^{-10} mol s^{-1} cm^{-2} and FE of 3.9% at −0.75 V *vs.* RHE in 0.1 M Na_2SO_4, far outperforming the bare CuO or RGO alone. The highly stable and efficient mode for the N_2 adsorption activity of CuO was attributed to the (111) facet of surface end groups. Similarly, a-Au/CeO_x-RGO achieved a comparable NH_3 performance due to the amorphous Au, which has more structural distortion and a higher concentration of catalytic NRR active sites.[116] The alloyed Au_1Co_1 NPs dispersed on GO can also synergistically boost the activation of the N≡N bond, and its synergistic effect is mainly reflected in Au_1Co_1 (111) (Fig. 6c).[117]

G-Based materials are always modified by the introduction of defects[129] or heteroatoms[130] to improve their usage. Defective G disrupts the original electronic arrangement and improves the transfer of electrons from the electrocatalyst to the chemisorbed molecules. He's group prepared an ultrathin porous dopant-free defect G using the molten salt method (Fig. 6d).[131] It is noteworthy that the defect G utilizes the product NH_3 from the NRR instead of N_2 as the N source for N doping (Fig. 6e). G can also be activated by lone pairs of electrons in electron-rich dopants, or by empty orbitals in electron-deficient dopants, thereby destroying the integrity of π-conjugation.[132,133] Boron (B) is an effective doping example, which can cause electron deficiency in G and thus increase electrocatalytic activity.[134,135] The local electron-deficient environment at the B-doped site provides a powerful binding site for the Lewis base, leading to improved electrocatalytic activity. Recently, Zheng's group reported B-doped G. In this work, the distribution structures and

Open Access Article. Published on 13 1400. Downloaded on 14/02/1405 07:56:34 ..
This article is licensed under a Creative Commons Attribution-NonCommercial 3.0 Unported Licence.

contents of B have distinct effects on NH_3 yield and FE. Among the structure of BC_3, BC_2O and BCO_2, the G-like BC_3-type bond plays a key role in enhancing N_2 fixation. At a doping level of 6.2%, the B-doped G achieves an NH_3 production rate of 9.8 μg h^{-1} cm^{-2} and a remarkable FE of 10.8% at −0.5 V *vs.* RHE in aqueous solutions. B doping in the G framework leads to the redistribution of electron density, where the electron-deficient boron sites provide enhanced binding capability to N_2 molecules.[128] Wang's group developed B, N co-doped G with abundant defects by thermal treatment of GO and boric acid under an NH_3 atmosphere followed by annealing. Edge carbon atoms occurring near B–N pairs were found to be the active sites for the NRR. Thus, the NRR with a high NH_3 production rate (7.75 μg h^{-1} $mg_{cat.}^{-1}$) and excellent FE (13.79%) was achieved at −0.3 V *vs.* RHE.[136]

Analogous to G, the crystal structure of graphitic carbon nitride (C_3N_4) may be described as a hexagonal carbon framework with N-substituted carbon by the sp^2 hybridization of C and N atoms. C_3N_4 and related materials possess evenly distributed holes, a tunable electronic structure and uniform pyridinic-N coordinators rich in lone electron pairs able to capture metal ions in the ligands. C_3N_4 has a more negative conduction position relative to the reduction potential of N_2/NH_3, which favours the activation of adsorbed N_2.[137] The 2D C_3N_4-NV, which has a larger specific surface area and abundant NVs, has a lower reaction ΔG (Fig. 6f).[138] This is because NVs can enrich electrons and transfer them to the $2\pi^*$ orbital of N_2, thereby enhancing the adsorption effect.

MXenes have been widely reported in the electrocatalysis field due to their diverse metal active centres and abundant surface end groups.[139–141] For example, $Ti_3C_2T_x$ (T = F, OH),[142] $Ti_3C_2T_x$ (T = O, OH),[143] MXene/$TiFeO_x$-700,[144] and Ti_3C_2OH QDs[123] achieved good NRR activities by modifying the surface end groups. Li and co-workers developed small sized fluorine-free $Ti_3C_2T_x$ (T = O, OH) NSs for the NRR, synthesized by TMAOH intercalation and delamination.[143] The size effect and fluorine-free characteristics result in an NH_3 yield 1.8 times that of fluorine-based treatment. Tan's group reported a SAC Ru doped Mo_2CT_x NS material for the NRR in 0.5 M K_2SO_4, which increased the FE to 25.77%.[145] Among them, the SAC Ru is the main electron back-donation centre for the absorbance and activation of N_2 molecules.

4 Modification of nanomaterials

4.1 Forming alloy centres

N_2 activation is a complicated process. Although the single active site can activate N to a certain extent, it cannot balance well the adsorption energy of multiple reaction intermediate species. Extending the single active site to dual or multiple sites may further improve the overall NRR performance of the catalyst.

Bimetallic nanocatalysts have been introduced into NRR systems to enhance selectivity for N_2. In 2001, Jens K. Nørskov and co-workers reported a bimetallic ammonia synthesis strategy that used interpolation to find a rational catalyst in the periodic table.[146] They combined metals with high and low N_2 interaction energies to obtain the required interaction strength for preparation of NH_3 synthesis catalysts. By the introduction of N atoms to order the binary alloy, bimetallic catalysis could be achieved. Yu's group developed an amorphous BiNi alloy for the NRR, which was designed to activate N_2 molecules by optimizing the adsorption energy and adjusting the crystallinity.[147] The BiNi alloy has a significantly smaller area-specific impedance than Bi (Fig. 7c), indicating that the 3D nanoporous alloy framework promotes charge transport, thereby enhancing the NRR activity.

For metal–carbon-based materials, bimetallic alloying has been employed to alter such weak metal–carbon interactions into synergistic metal–metal interactions, thereby optimizing the electronic structure of monometals and accordingly, promoting the catalytic activity. Taking Pt/Au@ZIF as an example, ZIF electronically modified the d-band structure of the Pt/Au electrocatalyst and created electron deficient sites to achieve more favourable N adsorption of H (Fig. 7a).[36] According to the XPS spectra, after encapsulating the ZIF, the binding energy of Pt 4f shifts left and that of N 1s shifts right, clearly highlighting the electron density transfer from Pt to the ZIF framework by the Pt–N ZIF interaction (Fig. 7b). This electron migration from Pt to ZIF will form electron-deficient sites on the Pt surface, thereby forming N_2 adsorption sites. Moreover, the hydrophobic ZIF pores act as a barrier that prevents trace amounts of water from reaching the electrocatalytic sites, thereby inhibiting the HER. As a result, Pt/Au@ZIF has a FE >44 times that of Pt/Au (≈1%), and reaches a high NH_3 production rate of >161 μg h^{-1} $mg_{cat.}^{-1}$ under ambient conditions. AuCu/ZIF-8 was also reported for the NRR due to the large active surface areas and conductive carbon frameworks of the ZIF-8 precursor. The highly dispersed bimetallic active sites achieved an unprecedented NH_3 yield of 23.3 μg h^{-1} $mg_{cat.}^{-1}$.[35]

Due to the unique characteristics such as corrosion resistance under harsh conditions and adjustable performance (shorter distance between active sites facilitates component optimization), high-entropy alloys (HEAs) have also been applied in the NRR. The HEAs are synthesized by controlling the coordination entropy within 5 or more metal elements. Wang's group reported HEA RuFeCoNiCu NPs as a pH-universal NRR catalyst. When multiple H atoms are adsorbed, they are mainly distributed over the hollow positions, and the adsorption energy decreases rapidly with the H coverage.[148] Therefore, the surface H adsorption will affect the Co–Ni–Ni sites, but the optimal site of the NRR, t-Fe, is not at a hollow position and will not be affected significantly. Clearly, different metals may play different roles and work in a synergetic way to provide outstanding NRR performance (Fig. 7d). This catalyst has a surprising NH_3 yield of 57.1 μg h^{-1} $mg_{cat.}^{-1}$ at 0.05 V *vs.* RHE in 0.1 M KOH, and the corresponding FE is 38.5%. It also has excellent NRR activity in 0.1 M Li_2SO_4, 0.1 M Na_2SO_4, and 0.1 M HCl electrolytes.

4.2 Optimizing the valence state

N_2 activation is essentially an electron donating–accepting process between the catalyst surface and N_2 molecules. The

© 2021 The Author(s). Published by the Royal Society of Chemistry

Open Access Article. Published on 13 1400. Downloaded on 14/02/1405 07:56:34 ..
This article is licensed under a Creative Commons Attribution-NonCommercial 3.0 Unported Licence.

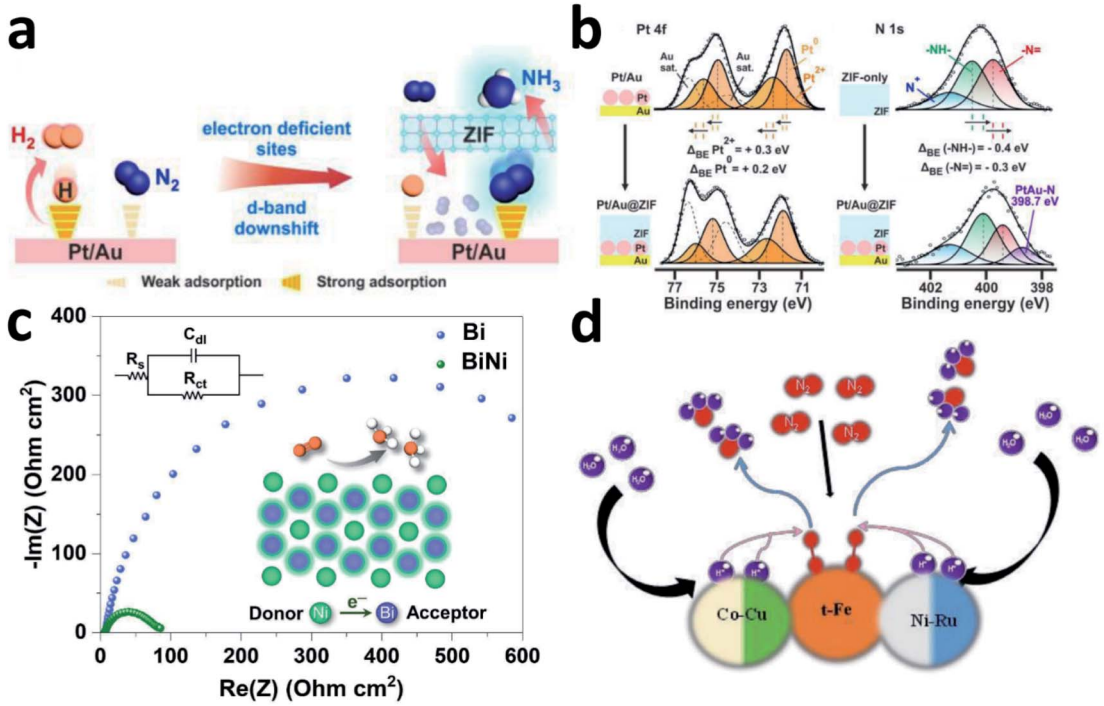

Fig. 7 (a) Schematic depicting the functions of Pt/Au@ZIF. (b) XPS investigations on the Pt/Au@ZIF platform. Copyright 2020, Wiley-VCH.[36] (c) EIS spectra of Bi and BiNi. Copyright 2020, Wiley-VCH.[147] (d) Schematic illustration of a possible mechanism of RuFeCoNiCu NPs. Copyright 2020, Wiley-VCH.[148]

different valence states for the active centre atoms will affect the energy barrier of the activation of N_2 molecules. Although both NbO_2 and Nb_2O_5 have similar octahedral structures, the catalytic properties differ significantly due to the different oxidation states of Nb (Fig. 8a). According to the report by Zheng's group, the FE of NbO_2 is almost 3.5 times higher than

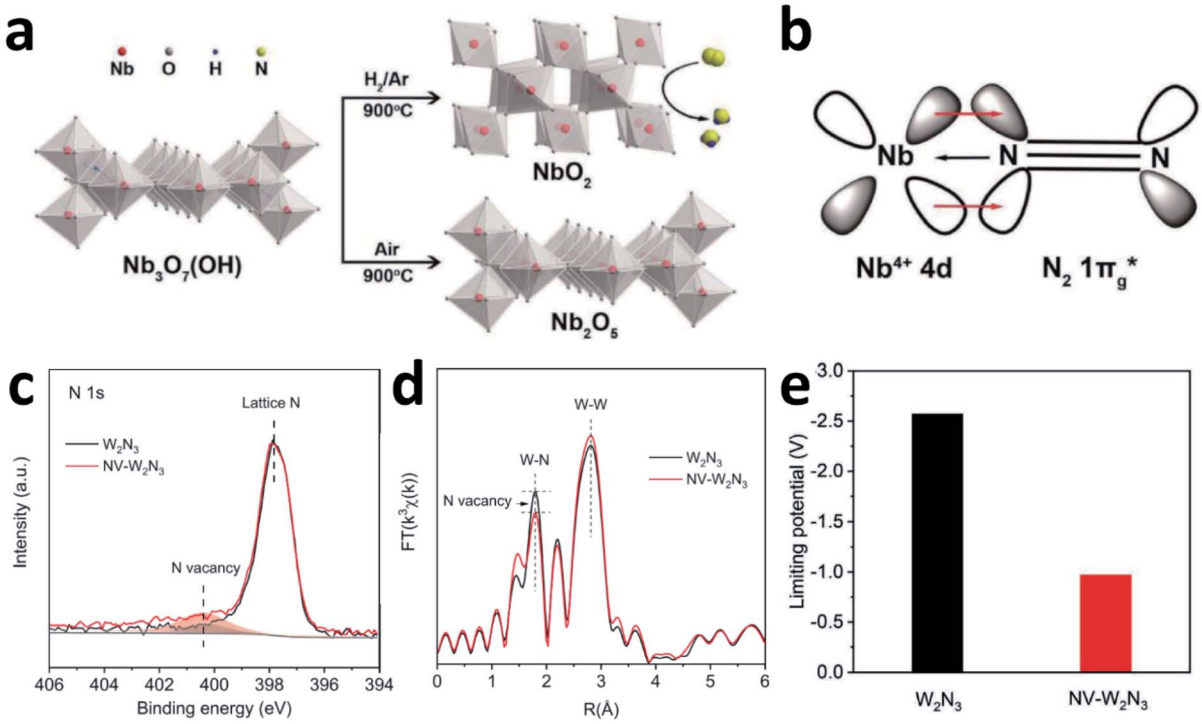

Fig. 8 (a) Synthetic schematic of NbO_2 and Nb_2O_5. (b) The interaction between Nb^{4+} and N_2. Copyright 2018, Wiley-VCH.[107] (c) N 1s spectra and (d) FT-EXAFS plots of the pristine W_2N_3 and NV-W_2N_3. (e) Magnitudes of the theoretical limiting potentials of NH_3 production on W_2N_3 and NV-W_2N_3. Copyright 2019, Wiley-VCH.[159]

Open Access Article. Published on 13 1400. Downloaded on 14/02/1405 07:56:34 ..
This article is licensed under a Creative Commons Attribution-NonCommercial 3.0 Unported Licence.

that of Nb_2O_5. For Nb_2O_5, the charge exchange and transfer mainly occur between the Nb atoms and N_2, and the electrons on the adjacent Nb atoms are transferred back to weaken the N≡N bond while strengthening the metal–N bond.[107] For NbO_2, the Jahn–Teller distortion destroys degeneracy, causing the t_{2g} level to split into partially occupied d_{xy} orbitals and partially unoccupied d_{yz} and d_{xz} orbitals. Therefore, when N_2 molecules are adsorbed on NbO_2, they not only bind electrons from its $3\sigma_g$ orbital to the empty orbital of Nb, but also accept d-electrons of Nb and back-donate to its anti-bonding $1\pi_g^*$ orbital (Fig. 8b). This back-donation can effectively weaken the N≡N bond and activate the adsorbed N_2 molecules. For Nb^{4+} with an electron occupying a 4d orbital, it should be easier to form such a back donor than Nb^{5+} without 4d electrons, so it exhibits better N_2 fixation activity.[24] Moreover, introducing mixed valences into nanomaterials to modulate the vacancy concentration and metal defect states could also induce the NRR process. Sun's group introduced Cu ions with mixed valences of +1 and +2 to modulate the defect states in TiO_2. Theoretical calculations suggest that when the Ti^{3+} $3d^1$ defect states present the splitting of e_g and t_{2g} orbitals, the adsorption and activation of N_2 enhanced strongly.[55]

4.3 Introducing vacancies

For a long time, surface chemical modifications like defect engineering and heteroatom doping have been regarded as efficient methods to boost NRR activity, due to the electronic structures of the electrochemical catalytic surfaces resulting in the modulation of adsorption properties.[149,150] Some introduced vacancy nanomaterials are summarized in Table 4.

4.3.1 Oxygen vacancies. Oxygen vacancies (OVs) with low formation energy are the most common anionic vacancies in transition metal oxides, which modulate the physicochemical properties of the material and thus influence the trapping and activation of inert N_2 molecules. $W_{18}O_{49}$ has exposed W sites and displays inherently weak binding of H_2, which is not conducive to the choice of N or H for the catalytic site. Fe doping modifies the surface atomic structure of $W_{18}O_{49}$ for effective NRR electrocatalysis and suppresses the HER. For the defect-rich $W_{18}O_{49}$, the abundant tunnels in its lattice structure make it ideal for heteroatom doping. Especially, compared to the d-spacing of $W_{18}O_{49}$ (3.8 Å), the size of Fe atoms (1.2 Å) would greatly facilitate their intercalation into $W_{18}O_{49}$. By changing the Fe doping level, the construction and surface properties of $W_{18}O_{49}$ can be finely tuned, which results in an increase in the number of OVs for exposing more W active sites, thereby enhancing the binding capability for N_2. Fe atoms are intercalated in the tunnels of $W_{18}O_{49}$, leading to the redistribution of the surface electrons of $W_{18}O_{49}$, thereby significantly minimizing the NRR overpotential, resulting in higher energy saving. The $W_{18}O_{49}$–16Fe@CFP attained a high NH_3 yield rate (24.7 $\mu g\ h^{-1}\ mg_{cat.}^{-1}$) and FE (20.0%) at a very low overpotential of −0.15 V *vs.* RHE.[82]

In contrast, Zhang's work anchored Fe atoms into OVs and doped Fe on the lattice, enhancing the adsorption and activation of N_2 on SnO_2 and improving the electrical conductivity of SnO_2, respectively.[170] This Fe–SnO_2 catalyst had a unique surface structure. In state of metallic Fe NPs or clusters, the elemental Fe in Fe–SnO_2 is composed of oxygen vacancy-anchored SAC Fe and lattice doped Fe, which largely lowered the energy barrier for activating chemically inert N_2 molecules. The electron paramagnetic resonance (EPR) spectra confirmed that many OVs existed within SnO_2 and Fe–SnO_2. However, the peak intensities of O 1s in the XPS and EPR spectra clearly decreased after Fe doping, which indicates that Fe may have

Table 4 Summary of introducing vacancy nanomaterials for the NRR

Catalyst[ref.]	Electrolyte	NH_3 yield ($\mu g\ h^{-1}\ mg_{cat.}^{-1}$)	NH_3 yield ($\times10^{-10}$ mol s^{-1} cm^{-2})	FE (%)	Potential (V *vs.* RHE)
OVs-Bi-VO_4 (ref. 151)	0.2 M Na_2SO_4	8.60	—	10.04	−0.50
OVs-MoO_2 (ref. 152)	0.1 M HCl	~12.20	—	8.20	−0.15
Bo-OV-MnO_2 (ref. 153)	0.5 M $LiClO_4$	54.2	—	16.80 (−0.20 V)	−0.40
Au@CeO_2 (ref. 58)	0.01 M H_2SO_4	10.60	4.61	9.50	−0.40
Al-doped Co_3O_4 (ref. 154)	0.1 M KOH	—	0.65	6.25	−0.20
OVs-CeO_2 (ref. 155)	0.1 M Na_2SO_4	16.4	—	3.70 (−0.40 V)	−0.50
Polymeric CN-NVx (ref. 156)	0.1 M HCl	8.09	—	11.59	−0.20
NVs-CN/C_{600} (ref. 157)	0.1 M HCl	2.9	—	16.8	−0.30
S-NVs-C_3N_4 (ref. 158)	0.5 M $LiClO_4$	32.7	—	14.1	−0.40
NVs-W_2N_3 NSs[159]	0.1 M KOH	11.66	0.38	11.67	−0.20
C_3N_4-NVs[138]	0.1 M HCl	17.85	—	10.96	−0.30
Vs-$FePS_3$ NSs[160]	0.1 M HCl	38.8	0.63	12.36 (−0.20 V)	−0.25
B-doped VS_2 (ref. 161)	0.5 M $LiClO_4$	55.7	—	16.40 (−0.20 V)	−0.40
Mo–SnS_2-SVs[162]	0.5 M $LiClO_4$	41.3	—	20.80 (−0.40 V)	−0.50
MoS_3-SVs[163]	0.5 M $LiClO_4$	51.7	—	12.8	−0.30
MoS_2-SVs[164]	0.1 M HCl	23.38	—	17.9	−0.35
Sb_2S_3-SVs[165]	0.1 M Na_2SO_4	10.85	—	3.75 (−0.30 V)	−0.40
N-doped MoS_2 (ref. 166)	0.1 M Na_2SO_4	69.82	—	9.14	−0.30
CoS_{1-x} (ref. 167)	0.05 M $H1_2SO_4$	~12.1	—	~16.5	−0.15
SV-1T-MoS_2@MoO_3 (ref. 168)	0.05 M H_2SO_4	116.1	—	18.9	−0.20
SVs-ZnS-rGO[169]	0.1 M HCl	51.2	—	28.2 (−0.10 V)	−0.15

© 2021 The Author(s). Published by the Royal Society of Chemistry

Open Access Article. Published on 13 1400. Downloaded on 14/02/1405 07:56:34 ..
This article is licensed under a Creative Commons Attribution-NonCommercial 3.0 Unported Licence.

been anchored by OVs. The extended X-ray absorption fine structure (EXAFS) of the catalyst showed a first-shell Fe–O contribution with a coordination number of about 3.6 at 2.01 Å, and a first-shell Fe–Sn contribution with a coordination number of about 0.4 at 3.12 Å, corresponding to lattice doped Fe. Moreover, the first-shell Fe–Sn contribution with a coordination number of about 4.4 at 3.87 Å can be ascribed to Fe anchored at OVs, forming a Sn–Fe–Sn structure. Therefore, the elemental Fe in Fe–SnO_2 can be categorized into isolated single-atom Fe on the surface with OVs, and lattice doped Fe. Consequently, the Fe–SnO_2 catalyst exhibited superior catalytic performance with a high NH_3 yield of 82.7 $\mu g\ h^{-1}\ mg_{cat.}{}^{-1}$ and a high FE of 20.4%.

4.3.2 Nitrogen vacancies. Since nitrogen vacancies (NVs) exhibit the same situation as N atoms in N_2 and could affect the electronic and energy band structure in nanomaterials, NVs may also have an enhanced ability to activate N_2. The high N contents and layered structure of C_3N_4 could generate copious and homogeneously distributed NVs.[156] Compared to pristine C_3N_4, C_3N_4 with NVs has a higher NRR activity, which can be partly attributed to the improvement of N_2 chemical adsorption by the NVs. Compared to NV-C_3N_4, the filled S dopants could induce electronic modulation and break the $*N_2H$–$*NH_2$ scaling relation to effectively stabilize $*N_2H$ and destabilize $*NH_2$ on S-NV-C_3N_4, leading to more optimized adsorption of the NRR intermediates and a significantly reduced energy barrier.[158] S-NV-C_3N_4 with a high S dopant concentration of 5.2% exhibited a comparable NRR performance.

Qiao's group experimentally and theoretically studied the NVs on W_2N_3, which acts as an efficient and stable NRR catalyst.[159] NV-W_2N_3 NSs were prepared by annealing under an NH_3 atmosphere, and the NVs were generated by further annealing (5% H_2/Ar at 500 °C for 3 h). According to the XPS N 1s spectra and EXAFS (Fig. 8c and d), compared to the pristine W_2N_3 NSs, the intensity of the peak (NVs) in NV-W_2N_3 increased and the coordination number of the W–N bond decreased, proving that vacancies were created. The authors also claimed that the high valence state of W and the surface distortion induced by the 2D morphology contribute to the good stability of NV-W_2N_3. Based on the pristine W_2N_3 theoretical model, they investigated the effect of introducing NVs on N_2 activation. When N vacancies are involved, significant charge transfer is observed between W_2N_3 and the adsorbed N_2 molecule. More importantly, inducing NVs decreases the theoretical limiting potentials of NH_3 production significantly (Fig. 8e), which is convenient for the NRR.

4.3.3 Sulfur vacancies. The O and S elements have very similar chemical properties, so the sulfur vacancies (SVs) are also expected to influence NRR performance by inducing additional sites for N_2 adsorption and activation. Hou's group reported the synthesis of porous $FePS_3$ NSs with abundant S vacancies (SVs-$FePS_3$ NSs) by electrochemical exfoliation in an organic electrolyte followed by hydrogenation treatment in a 5% H_2/Ar atmosphere.[160] The Fe species in the SVs-$FePS_3$ NSs were confirmed to be the true active sites by addition of the SCN^- ion as a poisoning agent, which was illustrated during chronoamperometry. XPS and EPR confirmed the formation of SVs. Residual electrons that are restrained in the Vs are more likely to flow to the surrounding Fe atoms, which leads to a strong hydrogen attraction that can be induced by the delocalised electrons around the Fe atoms, thus promoting the hydrogenation of N_2. Electron delocalization of SVs also improved the conductivity of SVs-Sb_2S_3 and boosted the activation of N_2.[165] The B element could act as a promoter to optimize the NRR energetics of active sites. Li and co-workers co-introduced Vs and B-dopant into VS_2 basal planes to promote the activity and selectivity of the NRR.[161] Compared with unsaturated Vs (1.13 eV), B-dopant unsaturated Vs (B-u-V) greatly exhibit the lower first hydrogenation step barrier of $*N_2$–$*NNH$ (0.77 eV), thereby promoting the activation of N_2. Meanwhile, compared with the B-dopant (1.05 eV), B-u-V has a lower barrier of 0.77 eV in the last reaction step ($*NH_2/NH_3$), which is conducive to NH_3 formation and desorption. The metal dopants and SVs could also form multimeric catalytic sites *via* a side-on configuration, such as the Mo–SnS_2-SVs reported by Chu.[162] Mo–Sn–Sn trimer active sites from DFT calculations confirm that more electrons are accumulated in the Mo/SV region of Mo–SnS_2-SVs compared to SnS_2. In total, the Mo–Sn–Sn trimer back-donates 0.55|e| to $*N_2$ (0.37|e| + 0.09|e| + 0.09|e|) according to Mulliken charge analysis. Upon N_2 adsorption, the large number of accumulated electrons induced by these Mo/SVs can be readily transferred into the antibonding orbitals of the N_2 molecule, thereby weakening and dissociating the N≡N bond.

5 Summary and outlook

Due to the urgent need to solve energy problems and the great attraction of finding new energy materials, the NRR is considered to be the most effective strategy for industrial production of NH_3 under mild conditions. Over the past five years, researchers from various countries have explored some effective and promising active centres to boost the adsorption and activation of N_2, combined with some low-dimensional nanomaterial substrates with high specific surface area, abundant exposed active sites, and unique electronic morphology to improve the performance of the NRR. In this review, we have briefly discussed some advanced low-dimensional nanomaterials with various structures in the development of the NRR, and also mentioned approaches to catalyst design and characteristics. In pursuit of more practical NRR catalysts with higher activity and selectivity, we provide some prospects for future research.

(1) Combination of theoretical calculations and some advanced characterization techniques (like NMR, XAFS, *etc.*) with experiments. A series of catalysts has been obtained using the results of theoretical calculations. Moreover, the adsorption energy of different sites on the catalyst surface could be explored by atomic-scale NMR technology. Using these two methods to design NRR catalysts in a targeted manner can save researchers time in screening catalysts.

(2) Improvement of the material preparation method. Constructing small-sized catalysts with diatomic or polyatomic active centres and combining them with low-dimensional nanomatrices. The diatomic or polyatomic active centres can reasonably regulate the adsorption process of each

Open Access Article. Published on 13 1400. Downloaded on 14/02/1405 07:56:34 ..
This article is licensed under a Creative Commons Attribution-NonCommercial 3.0 Unported Licence.

intermediate product in the N_2 activation process. Compounding with low-dimensional nanosized substrates can effectively adjust the exposed crystal faces of the catalyst, which is convenient for researchers to screen for active crystal faces. High-porosity 3D nanomaterials also have comparable potential as suitable substrate supported catalysts.

(3) Some elements with mixed valences are selected as the components of the catalyst to adjust the defect concentration and metal defect valences. N_2 activation is essentially an electron donor–acceptor process between the catalyst surface and N_2 molecules. The different valences of the active centre atoms will affect the energy barrier for activation of N_2 molecules.

(4) Designing a strategy that combines defect engineering and heteroatom doping. Defect engineering and heteroatom doping can change the electronic structure of the electrochemical catalyst surface, enhance the electron cloud density of the active site, and promote the adsorption and activation of N_2.

Conflicts of interest

There are no conflicts to declare.

Acknowledgements

Financial support from the National Natural Science Foundation Committee of China (Distinguished Youth Scientists Project of 51026004), Research Foundation of State Key Lab (ZK201805 and ZK201717), Jiangsu Distinguished Professorship Program (2016) and Sanyo Chemical Co. Ltd is gratefully acknowledged.

References

1 S. Chu and A. Majumdar, *Nature*, 2012, **488**, 294–303.
2 G. Soloveichik, M. Acharya, H. Cheeseman, D. Wicks and D. Tew, *Renewable Energy to Fuels through Utilization of Energy-Dense Liquids (REFUEL)*, U.S. DOE, 2016.
3 V. Rosca, M. Duca, M. T. d. Groot and M. T. M. Koper, *Chem. Rev.*, 2009, **109**, 2209–2244.
4 L. Wang, M. Xia, H. Wang, K. Huang, C. Qian, C. T. Maravelias and G. A. Ozin, *Joule*, 2018, **2**, 1055–1074.
5 M. Kitano, Y. Inoue, Y. Yamazaki, F. Hayashi, S. Kanbara, S. Matsuishi, T. Yokoyama, S. W. Kim, M. Hara and H. Hosono, *Nat. Chem.*, 2012, **4**, 934–940.
6 R. Schlgl, *Angew. Chem., Int. Ed.*, 2003, **42**, 2004–2008.
7 B. E. Smith, R. L. Richards and W. E. Newton, *Catalysts for Citrogen Fixation*, 2004.
8 J. A. Pool, E. Lobkovsky and P. J. Chirik, *Nature*, 2004, **427**, 527–530.
9 Y. Wang, M. Craven, X. Yu, J. Ding, P. Bryant, J. Huang and X. Tu, *ACS Catal.*, 2019, **9**, 10780–10793.
10 H. Wang, H. Li, M. Zhang, Y. Song, J. Huang, H. Huang, M. Shao, Y. Liu and Z. Kang, *ACS Appl. Mater. Interfaces*, 2018, **10**, 16308–16314.
11 D. L. Nelson and M. M. Cox, *Chem. Educ.*, 2001, **6**, 69–70.
12 B. A. MacKay and M. D. Fryzuk, *Chem. Rev.*, 2004, **104**, 385–402.
13 J. S. Anderson, J. Rittle and J. C. Peters, *Nature*, 2013, **501**, 84–87.
14 J. Chatt, A. J. Pearman and R. L. Richards, *Nature*, 1975, **253**, 39–40.
15 V. A. A. Sclafani and M. Schiavello, *J. Electrochem. Soc.*, 1982, **130**, 735–737.
16 M. Kitano, J. Kujirai, K. Ogasawara, S. Matsuishi, T. Tada, H. Abe, Y. Niwa and H. Hosono, *J. Am. Chem. Soc.*, 2019, **141**, 20344–20353.
17 M. Hattori, S. Iijima, T. Nakao, H. Hosono and M. Hara, *Nat. Commun.*, 2020, **11**, 2001.
18 H. Liu, *Chin. J. Catal.*, 2014, **35**, 1619–1640.
19 C. J. van der Ham, M. T. Koper and D. G. Hetterscheid, *Chem. Soc. Rev.*, 2014, **43**, 5183–5191.
20 G. Hochman, A. S. Goldman, F. A. Felder, J. M. Mayer, A. J. M. Miller, P. L. Holland, L. A. Goldman, P. Manocha, Z. Song and S. Aleti, *ACS Sustainable Chem. Eng.*, 2020, **8**, 8938–8948.
21 H. Davy, *Philos. Trans. R. Soc. London*, 1807, **97**, 1–56.
22 S. Giddey, S. P. S. Badwal and A. Kulkarni, *Int. J. Hydrogen Energy*, 2013, **38**, 14576–14594.
23 R. Silverstein and W. A. Bulen, *Biochemistry*, 1970, **9**, 3809–3815.
24 L. Huang, J. Wu, P. Han, A. M. Al-Enizi, T. M. Almutairi, L. Zhang and G. Zheng, *Small Methods*, 2019, **3**, 1800386.
25 J. Feng and H. Pan, *J. Mater. Chem. A*, 2020, **8**, 13896–13915.
26 X. F. Li, Q. K. Li, J. Cheng, L. Liu, Q. Yan, Y. Wu, X. H. Zhang, Z. Y. Wang, Q. Qiu and Y. Luo, *J. Am. Chem. Soc.*, 2016, **138**, 8706–8709.
27 M. A. Shipman and M. D. Symes, *Catal. Today*, 2016, **286**, 57–68.
28 J. Humphreys, R. Lan and S. Tao, *Advanced Energy and Sustainability Research*, 2020, **2**, 2000043.
29 H. Zhou, B. Xiong, L. Chen and J. Shi, *J. Mater. Chem. A*, 2020, **8**, 20286–20293.
30 Y. Yao, S. Zhu, H. Wang, H. Li and M. Shao, *J. Am. Chem. Soc.*, 2018, **140**, 1496–1501.
31 Y. Yao, S. Zhu, H. Wang, H. Li and M. Shao, *Angew. Chem., Int. Ed.*, 2020, **59**, 10479–10483.
32 S. Liu, T. Qian, M. Wang, H. Ji, X. Shen, C. Wang and C. Yan, *Nat. Catal.*, 2021, **4**, 322–331.
33 B. L. Li, M. I. Setyawati, H. L. Zou, J. X. Dong, H. Q. Luo, N. B. Li and D. T. Leong, *Small*, 2017, **13**, 1700527.
34 X. Yang, F. Ling, J. Su, X. Zi, H. Zhang, H. Zhang, J. Li, M. Zhou and Y. Wang, *Appl. Catal., B*, 2020, **264**, 118477.
35 X. Lv, L. Wang, G. Wang, R. Hao, J. Ren, X. Liu, P. N. Duchesne, Y. Liu, W. Li, Z. Yuan and G. A. Ozin, *J. Mater. Chem. A*, 2020, **8**, 8868–8874.
36 H. Y. F. Sim, J. R. T. Chen, C. S. L. Koh, H. K. Lee, X. Han, G. C. Phan-Quang, J. Y. Pang, C. L. Lay, S. Pedireddy, I. Y. Phang, E. K. L. Yeow and X. Y. Ling, *Angew. Chem., Int. Ed.*, 2020, **59**, 16997–17003.
37 C. Chen, C. Liang, J. Xu, J. Wei, X. Li, Y. Zheng, J. Li, H. Tang and J. Li, *Electrochim. Acta*, 2020, **335**, 135708.
38 Y. Liu, L. Huang, X. Zhu, Y. Fang and S. Dong, *Nanoscale*, 2020, **12**, 1811–1816.

© 2021 The Author(s). Published by the Royal Society of Chemistry

Open Access Article. Published on 13 1400. Downloaded on 14/02/1405 07:56:34 ..
This article is licensed under a Creative Commons Attribution-NonCommercial 3.0 Unported Licence.

39 H. Xian, H. Guo, Z. Chen, G. Yu, A. A. Alshehri, K. A. Alzahrani, F. Hao, R. Song and T. Li, *ACS Appl. Mater. Interfaces*, 2020, **12**, 2445–2451.
40 C. Wang, X. Zhu and P. Zuo, *Chem. Eng. J.*, 2020, **396**, 125163.
41 T. Xu, D. Ma, C. Li, Q. Liu, S. Lu, A. M. Asiri, C. Yang and X. Sun, *Chem. Commun.*, 2020, **56**, 3673–3676.
42 S. Luo, X. Li, M. Wang, X. Zhang, W. Gao, S. Su, G. Liu and M. Luo, *J. Mater. Chem. A*, 2020, **8**, 5647–5654.
43 W. Xu, G. Fan, J. Chen, J. Li, L. Zhang, S. Zhu, X. Su, F. Cheng and J. Chen, *Angew. Chem., Int. Ed.*, 2020, **59**, 3511–3516.
44 W. Tong, B. Huang, P. Wang, L. Li, Q. Shao and X. Huang, *Angew. Chem., Int. Ed.*, 2020, **59**, 2649–2653.
45 S. Xiao, F. Luo, H. Hu and Z. Yang, *Chem. Commun.*, 2020, **56**, 446–449.
46 X. Li, T. Li, Y. Ma, Q. Wei, W. Qiu, H. Guo, X. Shi, P. Zhang, A. M. Asiri, L. Chen, B. Tang and X. Sun, *Adv. Energy Mater.*, 2018, **8**, 1801357.
47 C. Wang, J. Gao, J. Zhao, D. Yan and X. Zhu, *Small*, 2020, **16**, 1907091.
48 Y. T. Liu, D. Li, J. Yu and B. Ding, *Angew. Chem., Int. Ed.*, 2019, **58**, 16439–16444.
49 Z. Geng, Y. Liu, X. Kong, P. Li, K. Li, Z. Liu, J. Du, M. Shu, R. Si and J. Zeng, *Adv. Mater.*, 2018, **30**, e1803498.
50 S. Zhang, M. Jin, T. Shi, M. Han, Q. Sun, Y. Lin, Z. Ding, L. R. Zheng, G. Wang, Y. Zhang, H. Zhang and H. Zhao, *Angew. Chem., Int. Ed.*, 2020, **59**, 13423–13429.
51 J. Li, S. Chen, F. Quan, G. Zhan, F. Jia, Z. Ai and L. Zhang, *Chem*, 2020, **6**, 885–901.
52 S. Mukherjee, X. Yang, W. Shan, W. Samarakoon, S. Karakalos, D. A. Cullen, K. More, M. Wang, Z. Feng, G. Wang and G. Wu, *Small Methods*, 2020, **4**, 1900821.
53 L. Han, X. Liu, J. Chen, R. Lin, H. Liu, F. Lu, S. Bak, Z. Liang, S. Zhao, E. Stavitski, J. Luo, R. R. Adzic and H. L. Xin, *Angew. Chem., Int. Ed.*, 2019, **58**, 2321–2325.
54 K. Jia, Y. Wang, Q. Pan, B. Zhong, Y. Luo, G. Cui, X. Guo and X. Sun, *Nanoscale Adv.*, 2019, **1**, 961–964.
55 T. Wu, H. Zhao, X. Zhu, Z. Xing, Q. Liu, T. Liu, S. Gao, S. Lu, G. Chen, A. M. Asiri, Y. Zhang and X. Sun, *Adv. Mater.*, 2020, **32**, e2000299.
56 J. Dong, J. Han, Y. Liu, A. Nakajima, S. Matsushita, S. Wei and W. Gao, *ACS Appl. Mater. Interfaces*, 2014, **6**, 1385–1388.
57 T. Montini, M. Melchionna, M. Monai and P. Fornasiero, *Chem. Rev.*, 2016, **116**, 5987–6041.
58 G. Liu, Z. Cui, M. Han, S. Zhang, C. Zhao, C. Chen, G. Wang and H. Zhang, *Chem.–Eur. J.*, 2019, **25**, 5904–5911.
59 W. Li, C. Zhang, M. Han, Y. Ye, S. Zhang, Y. Liu, G. Wang, C. Liang and H. Zhang, *ACS Appl. Mater. Interfaces*, 2019, **11**, 44186–44195.
60 M. M. Shi, D. Bao, B. R. Wulan, Y. H. Li, Y. F. Zhang, J. M. Yan and Q. Jiang, *Adv. Mater.*, 2017, **29**, 1606550.
61 Z. H. Xue, S. N. Zhang, Y. X. Lin, H. Su, G. Y. Zhai, J. T. Han, Q. Y. Yu, X. H. Li, M. Antonietti and J. S. Chen, *J. Am. Chem. Soc.*, 2019, **141**, 14976–14980.
62 X. Xu, X. Tian, B. Sun, Z. Liang, H. Cui, J. Tian and M. Shao, *Appl. Catal., B*, 2020, **272**, 118984.
63 Z. Liu, T. Huang, H. Chang, F. Wang, J. Wen, H. Sun, M. Hossain, Q. Xie, Y. Zhao and Y. Wu, *Energy Environ. Mater.*, 2020, **4**, 255–262.
64 Y. Zhai, Z. Zhu, C. Zhu, K. Chen, X. Zhang, J. Tang and J. Chen, *Mater. Today*, 2020, **38**, 99–113.
65 Y. Qiu, X. Peng, F. Lü, Y. Mi, L. Zhuo, J. Ren, X. Liu and J. Luo, *Chem.–Asian J.*, 2019, **14**, 2770–2779.
66 A. Wang, J. Li and T. Zhang, *Nat. Rev. Chem.*, 2018, **2**, 65–81.
67 Q. Qin, T. Heil, M. Antonietti and M. Oschatz, *Small Methods*, 2018, **2**, 1800202.
68 X. W. Guo, S. M. Chen, H. J. Wang, Z. M. Zhang, H. Lin, L. Song and T. B. Lu, *J. Mater. Chem. A*, 2019, **7**, 19831–19837.
69 H. Tao, C. Choi, L. X. Ding, Z. Jiang, Z. Han, M. Jia, Q. Fan, Y. Gao, H. Wang, A. W. Robertson, S. Hong, Y. Jung, S. Liu and Z. Sun, *Chem*, 2019, **5**, 204–214.
70 Q. Wei, F. Xiong, S. Tan, L. Huang, E. H. Lan, B. Dunn and L. Mai, *Adv. Mater.*, 2017, **29**, 1602300.
71 Q. Zhao, M. Zhao, J. Qiu, W. Y. Lai, H. Pang and W. Huang, *Small*, 2017, **13**, 1701091.
72 L. Zhang, P. Lu, Y. Luo, J. Y. Zheng, W. Ma, L. Ding and H. Wang, *J. Mater. Chem. A*, 2021, **9**, 9609–9615.
73 X. Li and J. Wang, *InfoMat*, 2019, **2**, 3–32.
74 J. Wen, H. Chang, T. Huang, M. Hossain, Z. Liu, H. Sun, Y. Zhu, Y. Chen, Q. Huang and Y. Wu, *Electrochim. Acta*, 2020, **367**, 137421.
75 N. Zhang, L. Li, J. Wang, Z. Hu, Q. Shao, X. Xiao and X. Huang, *Angew. Chem., Int. Ed.*, 2020, **59**, 8066–8071.
76 S. Chen, S. Perathoner, C. Ampelli, C. Mebrahtu, D. Su and G. Centi, *Angew. Chem., Int. Ed.*, 2017, **56**, 2699–2703.
77 J. Han, Z. Liu, Y. Ma, G. Cui, F. Xie, F. Wang, Y. Wu, S. Gao, Y. Xu and X. Sun, *Nano Energy*, 2018, **52**, 264–270.
78 H. Wang, D. Yang, S. Liu, S. Yin, Y. Xu, X. Li, Z. Wang and L. Wang, *ACS Sustainable Chem. Eng.*, 2019, **7**, 15772–15777.
79 F. Lai, W. Zong, G. He, Y. Xu, H. Huang, B. Weng, D. Rao, J. A. Martens, J. Hofkens, I. P. Parkin and T. Liu, *Angew. Chem., Int. Ed.*, 2020, **59**, 13320–13327.
80 B. Li, X. Zhu, J. Wang, R. Xing, Q. Liu, X. Shi, Y. Luo, S. Liu, X. Niu and X. Sun, *Chem. Commun.*, 2020, **56**, 1074–1077.
81 Y. T. Liu, X. Chen, J. Yu and B. Ding, *Angew. Chem., Int. Ed.*, 2019, **58**, 18903–18907.
82 Y. Tong, H. Guo, D. Liu, J. Liang, X. Yan, P. Su, S. Zhou, J. Liu, G. Q. M. Lu and S. X. Dou, *Angew. Chem., Int. Ed.*, 2020, **59**, 7356–7361.
83 T. Huang, Z. Liu, Y. Zhang, F. Wang, J. Wen, C. Wang, M. Hossain, Q. Xie, S. Yao and Y. Wu, *J. Mater. Chem. A*, 2020, **8**, 13679–13684.
84 W. Q. Qiu, Y. L. Luo, R. L. Liang and J. D. Qiu, *Chemistry*, 2020, **26**, 10226–10229.
85 Y. Wang, X. Cui, J. Zhao, G. Jia, L. Gu, Q. Zhang, L. Meng, Z. Shi, L. Zheng, C. Wang, Z. Zhang and W. Zheng, *ACS Catal.*, 2018, **9**, 336–344.
86 M. Arif, G. Yasin, L. Luo, W. Ye, M. A. Mushtaq, X. Fang, X. Xiang, S. Ji and D. Yan, *Appl. Catal., B*, 2020, **265**, 118559.
87 X. Ren, J. Zhao, Q. Wei, Y. Ma, H. Guo, Q. Liu, Y. Wang, G. Cui, A. M. Asiri, B. Li, B. Tang and X. Sun, *ACS Cent. Sci.*, 2019, **5**, 116–121.

Open Access Article. Published on 13 1400. Downloaded on 14/02/1405 07:56:34 ..
This article is licensed under a Creative Commons Attribution-NonCommercial 3.0 Unported Licence.

88 C. Lv, C. Yan, G. Chen, Y. Ding, J. Sun, Y. Zhou and G. Yu, *Angew. Chem., Int. Ed.*, 2018, **57**, 6073–6076.
89 X. Wang, S. Qiu, J. Feng, Y. Tong, F. Zhou, Q. Li, L. Song, S. Chen, K. H. Wu, P. Su, S. Ye, F. Hou, S. X. Dou, H. K. Liu, G. Q. Max Lu, C. Sun, J. Liu and J. Liang, *Adv. Mater.*, 2020, **32**, e2004382.
90 X. Yang, F. Ling, X. Zi, Y. Wang, H. Zhang, H. Zhang, M. Zhou, Z. Guo and Y. Wang, *Small*, 2020, **16**, e2000421.
91 Y. Zhao, J. Liang, C. Wang, J. Ma and G. G. Wallace, *Adv. Energy Mater.*, 2018, **8**, 1702524.
92 C. G. Morales-Guio, L. A. Stern and X. Hu, *Chem. Soc. Rev.*, 2014, **43**, 6555–6569.
93 Q. Liu, X. Zhang, B. Zhang, Y. Luo, G. Cui, F. Xie and X. Sun, *Nanoscale*, 2018, **10**, 14386–14389.
94 X. Xiang, Z. Wang, X. Shi, M. Fan and X. Sun, *ChemCatChem*, 2018, **10**, 4530–4535.
95 X. Zhu, Z. Liu, Q. Liu, Y. Luo, X. Shi, A. M. Asiri, Y. Wu and X. Sun, *Chem. Commun.*, 2018, **54**, 11332–11335.
96 Z. Wang, K. Zheng, S. Liu, Z. Dai, Y. Xu, X. Li, H. Wang and L. Wang, *ACS Sustainable Chem. Eng.*, 2019, **7**, 11754–11759.
97 X. Ren, G. Cui, L. Chen, F. Xie, Q. Wei, Z. Tian and X. Sun, *Chem. Commun.*, 2018, **54**, 8474–8477.
98 P. Shen, Y. Liu, Q. Li and K. Chu, *Chem. Commun.*, 2020, **56**, 10505–10508.
99 H. Jin, C. Guo, X. Liu, J. Liu, A. Vasileff, Y. Jiao, Y. Zheng and S. Z. Qiao, *Chem. Rev.*, 2018, **118**, 6337–6408.
100 C. Chen, N. W. Li, B. Wang, S. Yuan and L. Yu, *Nanoscale Adv.*, 2020, **2**, 5496–5503.
101 L. Huang, Z. Hu, H. Jin, J. Wu, K. Liu, Z. Xu, J. Wan, H. Zhou, J. Duan, B. Hu and J. Zhou, *Adv. Funct. Mater.*, 2020, **30**, 1908486.
102 X. Xiao, H. Wang, P. Urbankowski and Y. Gogotsi, *Chem. Soc. Rev.*, 2018, **47**, 8744–8765.
103 M. Och, M. B. Martin, B. Dlubak, P. Seneor and C. Mattevi, *Nanoscale*, 2021, **13**, 2157–2180.
104 A. R. Singh, B. A. Rohr, J. A. Schwalbe, M. Cargnello, K. Chan, T. F. Jaramillo, I. Chorkendorff and J. K. Nørskov, *ACS Catal.*, 2016, **7**, 706–709.
105 L. Li, C. Tang, B. Xia, H. Jin, Y. Zheng and S. Z. Qiao, *ACS Catal.*, 2019, **9**, 2902–2908.
106 H. Cheng, L. X. Ding, G. F. Chen, L. Zhang, J. Xue and H. Wang, *Adv. Mater.*, 2018, **30**, e1803694.
107 M.-A. Légaré, G. Bélanger-Chabot, R. D. Dewhurst, E. Welz, I. Krummenacher, B. Engels and H. Braunschweig, *Science*, 2018, **359**, 896–900.
108 X. Zhang, T. Wu, H. Wang, R. Zhao, H. Chen, T. Wang, P. Wei, Y. Luo, Y. Zhang and X. Sun, *ACS Catal.*, 2019, **9**, 4609–4615.
109 Q. Liu, X. Zhang, J. Wang, Y. Zhang, S. Bian, Z. Cheng, N. Kang, H. Huang, S. Gu, Y. Wang, D. Liu, P. K. Chu and X. F. Yu, *Angew. Chem., Int. Ed.*, 2020, **59**, 14383–14387.
110 M. M. Shi, D. Bao, S. J. Li, B. R. Wulan, J. M. Yan and Q. Jiang, *Adv. Energy Mater.*, 2018, **8**, 1800124.
111 K. Chu, Y. Liu, Y. Li, H. Zhang and Y. Tian, *J. Mater. Chem. A*, 2019, **7**, 4389–4394.
112 H. Y. Zhou, J. C. Li, Z. Wen and Q. Jiang, *Phys. Chem. Chem. Phys.*, 2019, **21**, 14583–14588.
113 R. Zhao, C. Liu, X. Zhang, X. Zhu, P. Wei, L. Ji, Y. Guo, S. Gao, Y. Luo, Z. Wang and X. Sun, *J. Mater. Chem. A*, 2020, **8**, 77–81.
114 X. Zhang, Q. Liu, X. Shi, A. M. Asiri, Y. Luo, X. Sun and T. Li, *J. Mater. Chem. A*, 2018, **6**, 17303–17306.
115 F. Wang, Y. p. Liu, H. Zhang and K. Chu, *ChemCatChem*, 2019, **11**, 1441–1447.
116 S. J. Li, D. Bao, M. M. Shi, B. R. Wulan, J. M. Yan and Q. Jiang, *Adv. Mater.*, 2017, **29**, 1700001.
117 Q. Wang, G. Zheng, S. Hao, X. Liu, J. Zheng, Y. Wang, Z. Su, N. Xu, Y. He, L. Lei and X. Zhang, *ACS Sustainable Chem. Eng.*, 2019, **8**, 44–49.
118 H. Huang, F. Li, Q. Xue, Y. Zhang, S. Yin and Y. Chen, *Small*, 2019, **15**, 1903500.
119 P. Li, W. Fu, P. Zhuang, Y. Cao, C. Tang, A. B. Watson, P. Dong, J. Shen and M. Ye, *Small*, 2019, **15**, e1902535.
120 W. Qiu, X. Y. Xie, J. Qiu, W. H. Fang, R. Liang, X. Ren, X. Ji, G. Cui, A. M. Asiri, G. Cui, B. Tang and X. Sun, *Nat. Commun.*, 2018, **9**, 3485.
121 H. Wang, J. Wang, R. Zhang, C. Cheng, K. Qiu, Y. Yang, J. Mao, H. Liu, M. Du, C. Dong and X. Du, *ACS Catal.*, 2020, **10**, 4914–4921.
122 L. Zhang, L. X. Ding, G. F. Chen, X. Yang and H. Wang, *Angew. Chem., Int. Ed.*, 2019, **58**, 2612–2616.
123 Z. Jin, C. Liu, Z. Liu, J. Han, Y. Fang, Y. Han, Y. Niu, Y. Wu, C. Sun and Y. Xu, *Adv. Energy Mater.*, 2020, **10**, 2000797.
124 D. Liu, G. Zhang, Q. Ji, Y. Zhang and J. Li, *ACS Appl. Mater. Interfaces*, 2019, **11**, 25758–25765.
125 J. Su, H. Zhao, W. Fu, W. Tian, X. Yang, H. Zhang, F. ling and Y. Wang, *Appl. Catal., B*, 2020, **265**, 118589.
126 P. Chen, N. Zhang, S. Wang, T. Zhou, Y. Tong, C. Ao, W. Yan, L. Zhang, W. Chu, C. Wu and Y. Xie, *Proc. Natl. Acad. Sci. U. S. A.*, 2019, **116**, 6635–6640.
127 C. Li, Y. Fu, Z. Wu, J. Xia and X. Wang, *Nanoscale*, 2019, **11**, 12997–13006.
128 X. Yu, P. Han, Z. Wei, L. Huang, Z. Gu, S. Peng, J. Ma and G. Zheng, *Joule*, 2018, **2**, 1610–1622.
129 Y. Jiang, L. Yang, T. Sun, J. Zhao, Z. Lyu, O. Zhuo, X. Wang, Q. Wu, J. Ma and Z. Hu, *ACS Catal.*, 2015, **5**, 6707–6712.
130 W. Wei, H. Liang, K. Parvez, X. Zhuang, X. Feng and K. Mullen, *Angew. Chem., Int. Ed.*, 2014, **53**, 1570–1574.
131 Y. Du, C. Jiang, W. Xia, L. Song, P. Li, B. Gao, C. Wu, L. Sheng, J. Ye, T. Wang and J. He, *J. Mater. Chem. A*, 2020, **8**, 55–61.
132 Y. Li, Z. Zhou, P. Shen and Z. Chen, *ACA Nano*, 2009, **3**, 1952–1958.
133 S. Wang, L. Zhang, Z. Xia, A. Roy, D. W. Chang, J. B. Baek and L. Dai, *Angew. Chem., Int. Ed.*, 2012, **51**, 4209–4212.
134 Y. Zheng, Y. Jiao, L. Ge, M. Jaroniec and S. Z. Qiao, *Angew. Chem., Int. Ed.*, 2013, **52**, 3110–3116.
135 Y. Jiao, Y. Zheng, M. Jaroniec and S. Z. Qiao, *J. Am. Chem. Soc.*, 2014, **136**, 4394–4403.
136 C. Chen, D. Yan, Y. Wang, Y. Zhou, Y. Zou, Y. Li and S. Wang, *Small*, 2019, **15**, e1805029.
137 S. Wang, D. Guo, M. Zong, C. Fan, X. Jun and D.-H. Wang, *Appl. Catal., A*, 2021, **617**, 118112.

© 2021 The Author(s). Published by the Royal Society of Chemistry

Open Access Article. Published on 13 1400. Downloaded on 14/02/1405 07:56:34 ..
This article is licensed under a Creative Commons Attribution-NonCommercial 3.0 Unported Licence.

138 Z. Zhao, Y. Long, S. Luo, Y. Luo, M. Chen and J. Ma, *J. Energy Chem.*, 2021, **60**, 546–555.
139 B. Anasori, M. R. Lukatskaya and Y. Gogotsi, *Nat. Rev. Mater.*, 2017, **2**, 16098.
140 X. Guo, S. Lin, J. Gu, S. Zhang, Z. Chen and S. Huang, *Adv. Funct. Mater.*, 2020, **31**, 2008056.
141 Y. Luo, G. Chen, L. Ding, X. Chen, L. Ding and H. Wang, *Joule*, 2019, **3**, 279–289.
142 J. Zhao, L. Zhang, X. Y. Xie, X. Li, Y. Ma, Q. Liu, W. H. Fang, X. Shi, G. Cui and X. Sun, *J. Mater. Chem. A*, 2018, **6**, 24031–24035.
143 T. Li, X. Yan, L. Huang, J. Li, L. Yao, Q. Zhu, W. Wang, W. Abbas, R. Naz, J. Gu, Q. Liu, W. Zhang and D. Zhang, *J. Mater. Chem. A*, 2019, **7**, 14462–14465.
144 Y. Guo, T. Wang, Q. Yang, X. Li, H. Li, Y. Wang, T. Jiao, Z. Huang, B. Dong, W. Zhang, J. Fan and C. Zhi, *ACS Nano*, 2020, **14**, 9089–9097.
145 W. Peng, M. Luo, X. Xu, K. Jiang, M. Peng, D. Chen, T. S. Chan and Y. Tan, *Adv. Energy Mater.*, 2020, **10**, 2001364.
146 S. D. Claus, J. H. Jacobsen, B. S. Clausen, S. Bahn, A. Logadottir and J. K. Nørskov, *J. Am. Chem. Soc.*, 2001, **123**, 8404–8405.
147 Z. Fang, P. Wu, Y. Qian and G. Yu, *Angew. Chem., Int. Ed.*, 2021, **60**, 4275–4281.
148 D. Zhang, H. Zhao, X. Wu, Y. Deng, Z. Wang, Y. Han, H. Li, Y. Shi, X. Chen, S. Li, J. Lai, B. Huang and L. Wang, *Adv. Funct. Mater.*, 2020, **31**, 2006939.
149 Z. Xiao, C. Xie, Y. Wang, R. Chen and S. Wang, *J. Energy Chem.*, 2021, **53**, 208–225.
150 G. F. Chen, X. Cao, S. Wu, X. Zeng, L. X. Ding, M. Zhu and H. Wang, *J. Am. Chem. Soc.*, 2017, **139**, 9771–9774.
151 J. Yao, D. Bao, Q. Zhang, M. Shi, Y. Wang, R. Gao, J. Yan and Q. Jiang, *Small Methods*, 2019, **3**, 1800333.
152 G. Zhang, Q. Ji, K. Zhang, Y. Chen, Z. Li, H. Liu, J. Li and J. Qu, *Nano Energy*, 2019, **59**, 10–16.
153 K. Chu, Y. Liu, Y. Cheng and Q. Li, *J. Mater. Chem. A*, 2020, **8**, 5200–5208.
154 X. W. Lv, Y. Liu, R. Hao, W. Tian and Z. Y. Yuan, *ACS Appl. Mater. Interfaces*, 2020, **12**, 17502–17508.
155 B. Xu, L. Xia, F. Zhou, R. Zhao, H. Chen, T. Wang, Q. Zhou, Q. Liu, G. Cui, X. Xiong, F. Gong and X. Sun, *ACS Sustainable Chem. Eng.*, 2019, **7**, 2889–2893.
156 C. Lv, Y. Qian, C. Yan, Y. Ding, Y. Liu, G. Chen and G. Yu, *Angew. Chem., Int. Ed.*, 2018, **57**, 10246–10250.
157 G. Peng, J. Wu, M. Wang, J. Niklas, H. Zhou and C. Liu, *Nano Lett.*, 2020, **20**, 2879–2885.
158 K. Chu, Q. Li, Y. Liu, J. Wang and Y. Cheng, *Appl. Catal., B*, 2020, **267**, 118693.
159 H. Jin, L. Li, X. Liu, C. Tang, W. Xu, S. Chen, L. Song, Y. Zheng and S. Z. Qiao, *Adv. Mater.*, 2019, **31**, e1902709.
160 H. Wang, Z. Li, Y. Li, B. Yang, J. Chen, L. Lei, S. Wang and Y. Hou, *Nano Energy*, 2021, **81**, 105613.
161 Q. Li, Y. Guo, Y. Tian, W. Liu and K. Chu, *J. Mater. Chem. A*, 2020, **8**, 16195–16202.
162 K. Chu, J. Wang, Y. Liu, Q. Li and Y. Guo, *J. Mater. Chem. A*, 2020, **8**, 7117–7124.
163 K. Chu, H. Nan, Q. Li, Y. Guo, Y. Tian and W. Liu, *J. Energy Chem.*, 2021, **53**, 132–138.
164 M. You, S. Yi, X. Hou, Z. Wang, H. Ji, L. Zhang, Y. Wang, Z. Zhang and D. Chen, *J. Colloid Interface Sci.*, 2021, **599**, 849–856.
165 X. Wang, J. Bai, Y. Wang, X. Lu, Z. Zou, J. Huang and C. Xu, *Green Energy Environ.*, 2020, DOI: 10.1016/j.gee.2020.11.016.
166 L. Zeng, S. Chen, J. van der Zalm, X. Li and A. Chen, *Chem. Commun.*, 2019, **55**, 7386–7389.
167 C. Li, R. Xu, S. Ma, Y. Xie, K. Qu, H. Bao, W. Cai and Z. Yang, *Chem. Eng. J.*, 2021, **415**, 128958.
168 X. Zi, J. Wan, X. Yang, W. Tian, H. Zhang and Y. Wang, *Appl. Catal., B*, 2021, **286**, 119870.
169 J. Zhao, X. Liu, X. Ren, X. Sun, D. Tian, Q. Wei and D. Wu, *Appl. Catal., B*, 2021, **284**, 119746.
170 L. Zhang, M. Cong, X. Ding, Y. Jin, F. Xu, Y. Wang, L. Chen and L. Zhang, *Angew. Chem., Int. Ed.*, 2020, **59**, 10888–10893.